The short flagella 1 (SHF1) gene in *Chlamydomonas* encodes a Crescerin TOG-domain protein required for late stages of flagellar growth

Karina Perlaza, Mary Mirvis, Hiroaki Ishikawa, and Wallace Marshall*
Department of Biochemistry and Biophysics, University of California, San Francisco, San Francisco, CA 94143

ABSTRACT **Length control of flagella represents a simple and tractable system to investigate the dynamics of organelle size. Models for flagellar length control in the model organism *Chlamydomonas reinhardtii* have focused on the length dependence of the intraflagellar transport (IFT) system, which manages the delivery and removal of axonemal subunits at the tip of the flagella. One of these cargoes, tubulin, is the major axonemal subunit, and its frequency of arrival at the tip plays a central role in size control models. However, the mechanisms determining tubulin dynamics at the tip are still poorly understood. We discovered a loss-of-function mutation that leads to shortened flagella and found that this was an allele of a previously described gene, SHF1, whose molecular identity had not been determined. We found that SHF1 encodes a *Chlamydomonas* orthologue of Crescerin, previously identified as a cilia-specific TOG-domain array protein that can bind tubulin via its TOG domains and increase tubulin polymerization rates. In this mutant, flagellar regeneration occurs with the same initial kinetics as in wild-type cells but plateaus at a shorter length. Using a computational model in which the flagellar microtubules are represented by a differential equation for flagellar length combined with a stochastic model for cytoplasmic microtubule dynamics, we found that our experimental results are best described by a model in which Crescerin/SHF1 binds tubulin dimers in the cytoplasm and transports them into the flagellum. We suggest that this TOG-domain protein is necessary to efficiently and preemptively increase intraflagella tubulin levels to offset decreasing IFT cargo at the tip as flagellar assembly progresses.**

Monitoring Editor
Thomas Surrey
Centre for Genomic Regulation

Received: Sep 29, 2021
Revised: Nov 5, 2021
Accepted: Nov 16, 2021

INTRODUCTION

The complex structure of a eukaryotic cell can be broken down into a collection of distinct organelles, such that the question of cell architecture is reduced to the question of organelle size, shape, number, and position. The size of organelles can vary on a dynamic basis in response to external and internal signals (Chan and Marshall, 2012). The mechanisms by which organellar morphologies are maintained and transformed remain largely unknown. Measuring changes in organelle size is typically complicated by the inherently complex three-dimensional structures of many organelles, but the cilium or flagellum (used interchangeably) eases this technical barrier because the only parameter that varies is its length. By reducing the complexity to one dimension, it is easier to measure and model the dynamics of this protruding organelle (Wemmer and Marshall, 2007).

Eukaryotic flagella are appendages that extend from the surface of the cell. The flagellar membrane is continuous with the plasma membrane of the cell, but it is compartmentalized from the cytosol through the transition zone, a segment near the base of the flagella that acts as a protein diffusion barrier (Czarnecki and Shah, 2012). Because there are no ribosomes in flagella (Rosenbaum and Child, 1967), all flagellar structures must be assembled from precursor proteins synthesized in the cell body. Approximately 4–5% of the

This article was published online ahead of print in MBoC in Press (http://www.molbiolcell.org/cgi/doi/10.1091/mbc.E21-09-0472) on November 24, 2021.

*Address correspondence to: Wallace Marshall (wallace.ucsf@gmail.com).

Abbreviations used: IFT, intraflagellar transport; JBS, joubert syndrome; SHF1, short flagella gene 1; SNP, single nucleotide polymorphism; TAP, tris acetate phosphate; WGS, whole genome sequencing.

nuclear-encoded proteins made in the cell body are imported into the flagella (Pazour *et al.*, 2005). Flagellar assembly is accomplished through the addition of subunits at the distal tip (Rosenbaum and Child, 1967; Witman, 1975; Johnson and Rosenbaum, 1992). Because the axoneme, the core scaffold of the flagellum, is composed of nine doublet microtubules arranged in radial symmetry, tubulin subunits are critical for the assembly process. Flagellar length is determined by competing processes of assembly and disassembly both occurring at the flagellar distal tip (Johnson and Rosenbaum, 1992; Marshall and Rosenbaum, 2001; Song and Dentler, 2001). Assembly and disassembly rates are driven by the arrival of proteins at the tip and base of the flagella. The system dedicated to this bidirectional movement, intraflagellar transport (IFT), is responsible for moving select proteins along the axonemal microtubules via molecular motors (Kozminski *et al.*, 1993; Taschner *et al.*, 2016). Tubulin transported by the IFT system is mediated by specific binding sites for tubulins on specific IFT proteins (Bhogaraju *et al.*, 2013b, 2014; Kubo *et al.*, 2016; Taschner *et al.*, 2016), and tubulin can be visualized undergoing active IFT toward the assembly site at the tip (Hao *et al.*, 2011; Craft *et al.*, 2015).

Characterization of IFT dynamics has led to a simple "balance point" model that describes how steady-state flagellar length is set by a balance between assembly and disassembly rates (Marshall *et al.*, 2005). The disassembly rate has been found to be length independent, whereas the assembly rate decreases as the flagellum increases in length. IFT plays a major role in maintaining flagellar length because it balances the ongoing disassembly of the outer doublet microtubules by providing a constant supply of fresh subunits at the distal end. Reduction of IFT using temperature-sensitive mutants leads to reduction in steady-state flagellar length (Marshall and Rosenbaum, 2001; Marshall *et al.*, 2005; Engel *et al.*, 2012). Quantitative measurements show that the rate at which IFT particles enter the flagellum is a decreasing function of length (Engel *et al.*, 2012; Ludington *et al.*, 2013) such that as flagella elongate, the assembly rate will decrease until it exactly balances the disassembly rate, resulting in a unique steady-state length. Another model derived for flagellar length control is based on differential cargo loading by IFT. In this model, regulation of the cargo size transported by IFT particles is a decreasing function of length (Wren *et al.*, 2013) such that the cargo-carrying capacity is low in steady-state flagella and high during growth of new flagella.

The crux of these and most flagellar size control models is centered primarily around IFT dynamics. However, other work has pointed to regulation of the cytoplasmic precursor pool as an additional parameter that is crucial for proper size control (Rosenbaum *et al.*, 1969; Lefebvre *et al.*, 1978; Jarvik *et al.*, 1984). Tubulin is thought to be the limiting protein component of the precursor pool, supported by experiments showing that competition between flagella and cytoplasmic microtubules for a fixed pool of tubulin affects flagellar length. During flagellar regeneration, cytoplasmic microtubules undergo transient shortening, suggesting that tubulin is depleted and used for building the flagellum (Wang *et al.*, 2013). Loss-of-function in either kinesin 13, a microtubule depolymerizer located in the cell body (Piao *et al.*, 2009; Wang *et al.*, 2013), or katanin, a cytoplasmic microtubule-severing protein (Qasim Rasi *et al.*, 2009; Kannegaard *et al.*, 2014), both lead to shorter flagellar length. These mutant phenotypes can be explained if these microtubule disassembly factors normally act to shift cytosolic microtubule dynamics during flagellar formation so as to favor a more readily available tubulin pool. When these genes are mutated, cytoplasmic microtubules are more stable, and flagella become shorter because they cannot access the cytoplasmic tubulin pool.

Much of what is known about flagellar length, assembly, and precursor pools has come about through use of the model organism *Chlamydomonas reinhardtii*. This green unicellular alga has two flagella of equal lengths (10–12 µm) that can easily be detached through pH shock, after which the flagella regenerate back to normal length. *Chlamydomonas* can be grown as a haploid or diploid and has genetics similar to that of budding yeast. The ability to easily perform forward genetic screens in *Chlamydomonas* has led to the discovery of many mutants with abnormal flagellar lengths. Length-altering phenotypes in *Chlamydomonas* include diverse phenotypes such as short-flagella (shf), long-flagella (lf), and unequal-length flagella (ulf) (McVittie, 1972; Jarvik *et al.*, 1984; Barsel *et al.*, 1988; Asleson and Lefebvre, 1998; Tam *et al.*, 2003). Although the genes affected in some of these mutants have been identified and characterized, usually by taking advantage of insertional mutagenesis strategies, in many cases the underlying genes remain unidentified due to the fact that the mutation was not tagged with an insertion. Identified length-altering genes described so far include components of the IFT system (Pazour *et al.*, 1998; Iomini *et al.*, 2001; Matsuura *et al.*, 2002; Lucker *et al.*, 2010; Dutcher *et al.*, 2012; Lin *et al.*, 2013), kinases that regulate IFT (Berman *et al.*, 2003; Tam *et al.*, 2003, 2007, 2013; Ludington *et al.*, 2013; Wemmer *et al.*, 2020), and cytoplasmic microtubule regulators (Piao *et al.*, 2009; Qasim Rasi *et al.*, 2009; Wang *et al.*, 2013; Kannegaard *et al.*, 2014). Until now, factors directly involved in the incorporation of tubulin into the growing flagellum itself have not been reported among the existing length mutants of *C. reinhardtii*. As a result, models for flagellar length have generally not included specific representation of active modulators of tubulin dynamics. Here, we use a genetic approach to show that a TOG-domain array protein of the Crescerin family is required to achieve proper flagellar length, and we propose that it does so by allowing flagella to continue growth by preemptively increasing tubulin levels at the tip earlier in flagellar regeneration.

RESULTS

Identification of a TOG domain–containing protein required for full flagellar length

During the course of screening mutants obtained from the Chlamydomonas Library Project (CLiP) (Li *et al.*, 2019), we found a mutant strain with shorter flagella than that of wild-type (WT) cells that we provisionally refer to as *shf-A* (Figure 1A). Flagella in these mutant cells were 4.91 ± 0.226 (SEM) µm shorter than WT cells (Figure 1B) but were not paralyzed because they were capable of swimming. After backcrossing the original mutant to WT, tetrad analysis showed that the mutation was due to a single Mendelian mutation based on the 2:2 segregation pattern of the shf phenotype. Although paromomycin resistance also segregated 2:2, confirming the presence of only one full cassette, the paromomycin resistance and shf phenotypes did not cosegregate with each other, indicating that the shf phenotype was not caused by the insertion of the resistance cassette into the *shf* gene. Given that insertional mutagenesis often leads to multiple and diverse types of genetic disruptions, that is, large insertions, deletions, single nucleotide polymorphisms (SNPs), and global genomic rearrangements (Li *et al.*, 2016), we took an unbiased approach to discovering the genetic mutation in question (Figure 1C). One of the offspring from the first cross was used to cross once more to WT. After the second cross, tetrads were analyzed and separated into two pools, one containing DNA of 20 *shf* phenotype–exhibiting spores and one containing DNA of 20 WT phenotype–exhibiting spores. This approach was used to randomize

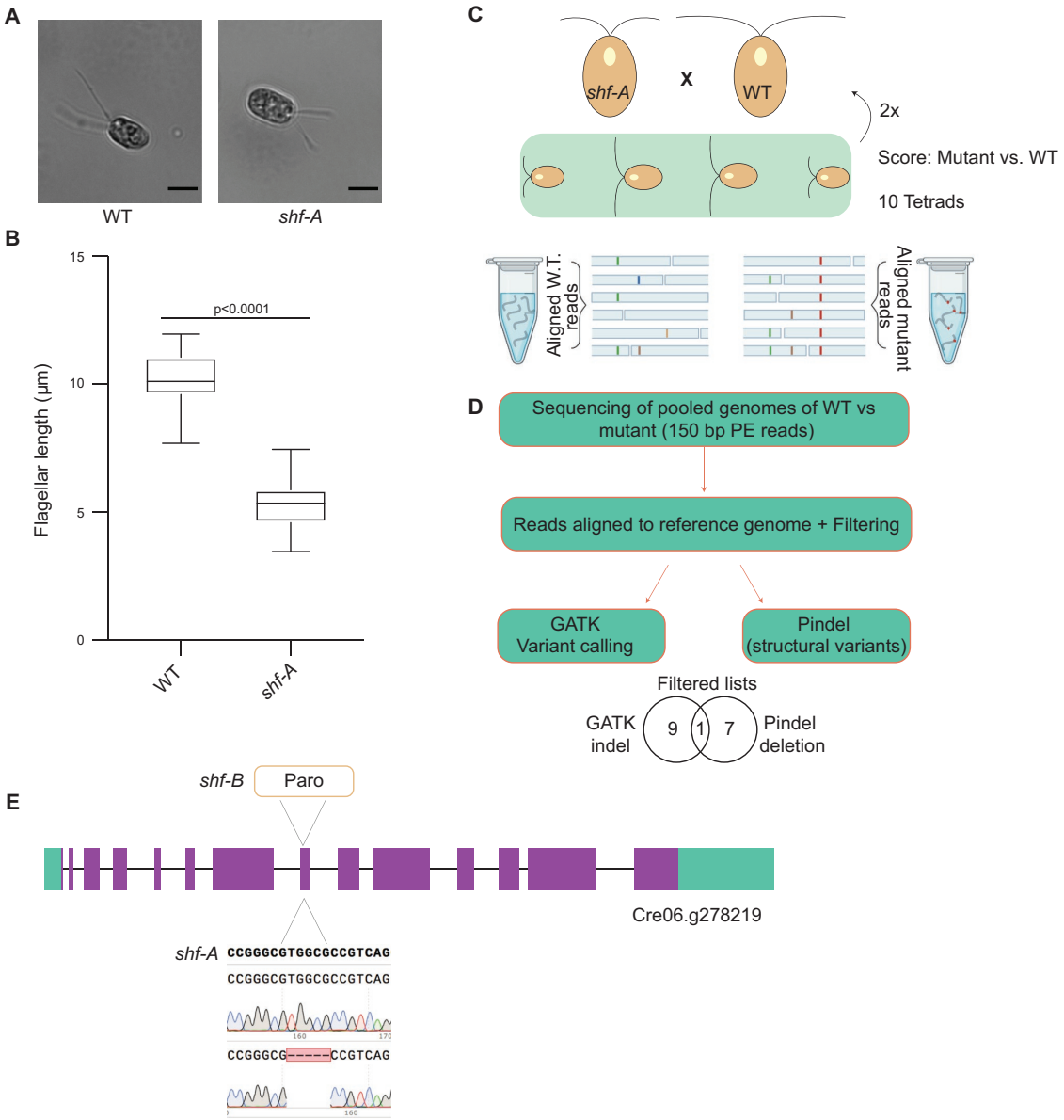

FIGURE 1: Discovery of a gene lesion resulting in short-flagellar phenotype. (A) Representative DIC images of WT (CC-125) and *shf-A Chlamydomonas* cells. Scale bar: 5 µm. (B) Box-and-whisker plot displaying flagellar-length data for WT ($n = 48$) and *shf-A* ($n = 50$) grown in alternating light and dark cycles in M1 media and subsequently fixed in glutaraldehyde. An unpaired *t* test was conducted to determine the *P* value ($p < 0.0001$). (C) Schematic showing our approach to discover the genetic lesion underpinning the short-flagellar phenotype. *shf-A* (mt-) was backcrossed to CC-125 (mt+), and then an *shf*-exhibiting offspring spore from this first cross was backcrossed once more to CC-125. The spores from tetrads and octads were scored for *shf* vs. WT flagellar lengths and separated into two different gDNA pools to enrich for the allele of interest. (D) Schematic describing the bioinformatic workflow for the mutational analysis. PE: Paired end, GATK: Genome Analysis Toolkit. (E) The diagram depicts the Cre06.g278219 gene with the green outermost boxes representing the 5′ untranslated region (5′UTR) and the 3′ untranslated region (3′UTR) from left to right, respectively. The purple boxes represent the exons, and the connecting black lines are the introns. The 5-base-pair deletion site for *shf-A* is shown through the Sanger sequencing chromatogram, whereas the insertion site of the mutagenic cassette (PARO) is indicated for the *shf-B* allele.

mutations specific to each background (WT vs. mutant) and enrich for the mutant allele of interest causing the *shf* phenotype. Using a modified bioinformatics workflow similar to that of Schierenbeck *et al.* (2015) (Figure 1D), we arrived at two filtered lists by variant calling algorithms, Pindel (structural variants, e.g., large deletions, insertions, inversions) and GATK (SNPs and Indels). Of the final filtered lists derived from each algorithm, one variant was found in both lists—a 5-base-pair deletion in exon 8 of gene Cre06.g278219 (Figure 1E). PCR of this region from tetrad products followed by Sanger sequencing confirmed the existence of the 5-base-pair deletion in spores showing the *shf-A* phenotype. The *shf* phenotype most likely results from a loss-of-function mutation because a 5-base-pair deletion would lead to an early stop codon. To increase our confidence that this was the causative allele of interest, we obtained a second, independently generated, mutant from the CLiP, which we found contained a paromomycin resistance cassette

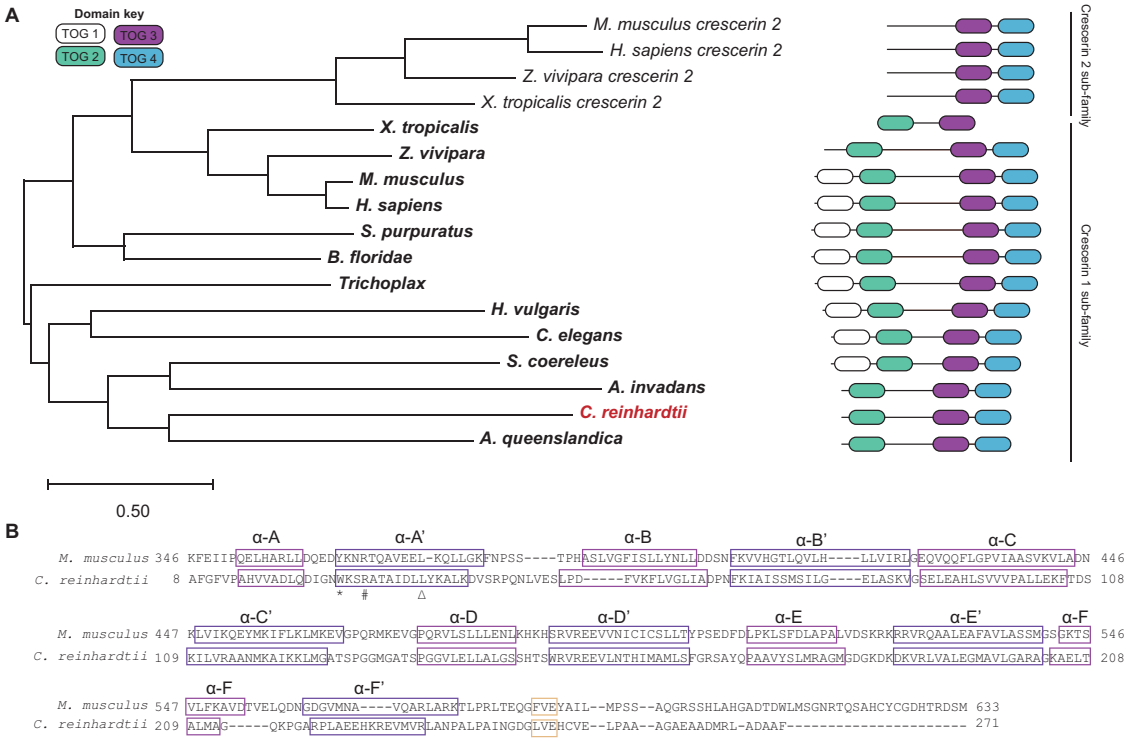

FIGURE 2: Cre06.g278219 encodes a conserved TOG-domain array protein. (A) The left side shows a cladogram depicting the relationships between Crescerin subfamilies. The tree is drawn to scale, with branch lengths measured in the number of substitutions per site. The right side shows the corresponding domain architectures for each organism. Each of the organisms' predicted domain structure and architecture are compared with the human TOG domains with all TOG domains and unstructured regions scaled to the human TOG-domain array-containing protein. TOG domains 1–4 are color coded as shown in the top left-side corner under the domain key. Supplemental_Table_1, sheet 3, contains the NCBI sequence identifiers for the Crescerin homologues used in this tree. (B) Amino acid sequence alignment of the Crescerin1 TOG2 domain of *M. musculus* and *C. reinhardtii* shows the archetypical structure of the TOG domain with six HEAT repeats (A–F) each containing a highly conserved alpha helical fold. The *M. musculus* crystal structure from Das *et al.* (2015) was used to demarcate the alpha helices in purple outlined rectangles, whereas a structural prediction program, PSIPRED, was used for the *C. reinhardtii* sequence. The yellow box highlights part of a unique beta-hairpin of the Crescerin protein (Das *et al.*, 2015) that differentiates it from other TOG-domain proteins. The residue number for each Crescerin sequence is shown to the left of the residues. An asterisk (*) underneath the sequence alignment indicates a conserved residue critical for binding to tubulin in both Crescerin (Das *et al.*, 2015) and other TOG-domain array proteins like CLASP and XMAP215 (Al-Bassam and Chang, 2011). The pound sign (#) underneath the sequence alignment indicates a residue that was found to be mutated in ciliopathies (Latour *et al.*, 2020; Morbidoni *et al.*, 2021). Finally, the triangle (Δ) underneath the sequence alignment highlights a residue found mutated in JBS ciliopathy patients (Latour *et al.*, 2020).

insertion in the exact location where the 5-base-pair deletion started (Figure 1E). This mutant, *shf-B*, phenocopied the *shf* phenotype of our original mutant (Supplemental Figure 1, A and B), *shf-A*, thus increasing our confidence that this gene, Cre06.g278219, is crucial in maintaining flagellar length.

The mutated gene, Cre06.g278219, designated as sensory, structural and assembly 6 (SSA6) in the *C. reinhardtii* genome database (Merchant *et al.*, 2007) is a homologue of the Crescerin1/CHE-12 gene. CHE-12 was first characterized in *Caenorhabditis elegans*, when it was observed that *che-12* worms exhibited abnormal *che*motaxis in response to sodium chloride (Bacaj *et al.*, 2008). Furthermore, *che-12* mutants had a cilia formation defect in a subset of sensory neurons. The human homologue, TOGARAM1 (later renamed Crescerin for the Latin *crescere*, to grow), belongs to a large family conserved across ciliated eukaryotes (Das *et al.*, 2015). Recently, TOGARAM1/Crescerin variants were shown to cause Joubert syndrome (JBS), a recessive neurodevelopmental ciliopathy (Latour *et al.*, 2020; Morbidoni *et al.*, 2021). TOGARAM1/Crescerin is a TOG (tumor overexpressed gene) domain array–containing protein that regulates cilia microtubule structure. TOG domains bind tubulin and have been shown to promote microtubule polymerization (Brouhard *et al.*, 2008; Fox *et al.*, 2014; Das *et al.*, 2015; Byrnes and Slep, 2017), raising the possibility that the *shf-A* mutant phenotype might reflect a role for microtubule growth dynamics in flagellar length control.

To examine the potential function of Crescerin in flagellar length regulation, we analyzed Crescerin protein domain structure and evolutionary conservation via phylogenetic analysis and sequence alignment. Previous analysis revealed two Crescerin subfamilies, Crescerin1 and Crescerin2 (Das *et al.*, 2015). We found that, whereas Crescerin2 is specific to vertebrates, Crescerin1 exists in both vertebrates and invertebrates (Figure 2A). Interestingly, our BLAST searches revealed no clear Crescerin1 homologue in plants, even in nonvascular plants such as liverworts, hornworts, and mosses closest to ancestral green algae, which contain motile cilia in their sperm. This result suggests that the sperm flagella in Bryophytes do not require Crescerin1 for proper assembly and function. Sequence alignments and structural predictions of homologues in other organisms indicate that the minimal unit of the Crescerin1 subfamily

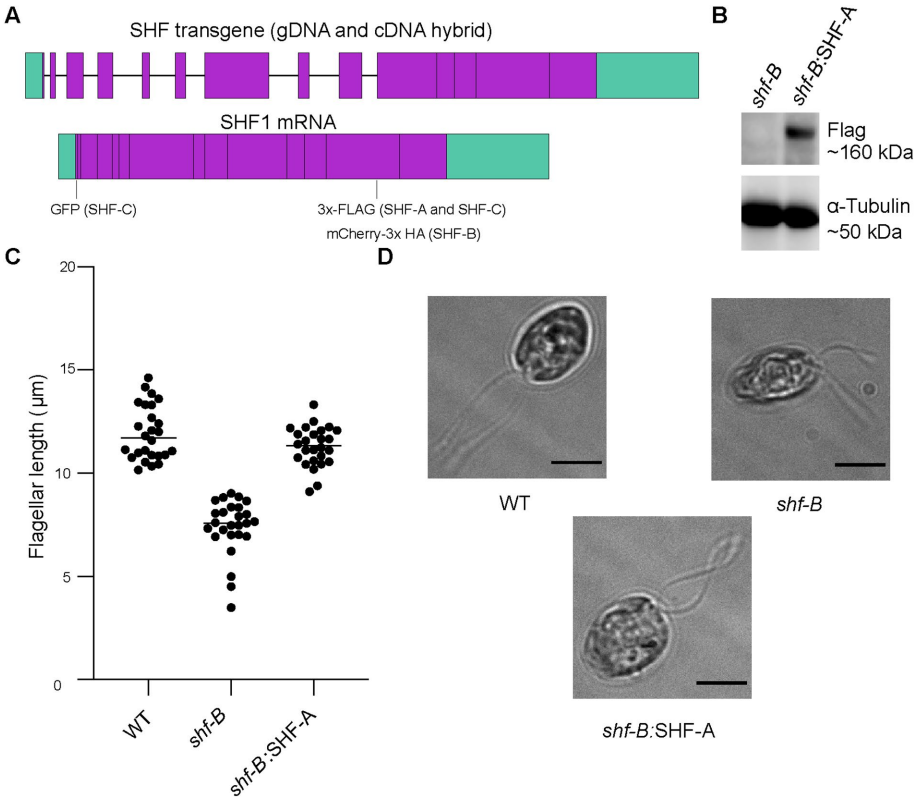

FIGURE 3: Expression of Crescerin transgene leads to rescue of short-flagellar phenotype. (A) The top panel shows the SHF transgene designed in the form of a gDNA and cDNA hybrid. The left green outermost rectangle depicts the 5′ untranslated region (UTR), whereas the right green outermost rectangle is the 3′ UTR. The first part of the transgene contains exons and introns 1–9, and the rest of the transgene is strictly exonic regions 10–16. In both the top and bottom panels, the horizontal lines demarcate the exon boundaries. The bottom panel shows the SHF-coding region and the different variety of transgenes used in this study: SHF-A, SHF-B, and SHF-C. The positions of the epitopes and/or fluorescent proteins for the different transgene constructs are shown. The 3x-FLAG epitope in SHF-A and SHF-C, mCherry-3x-HA in SHF-B, and the GFP in SHF-C. (B) Immunoblot analysis of samples prepared from strains *shf-B* and *shf-B*:SHF-A, a transformant selected for its WT-like length. Detection was done with antibodies against Flag (SHF-A), and α-tubulin (loading control). (C) Flagellar lengths were measured for each strain ($n = 26$) grown in TAP media. The horizontal line represents the median length of each strain. (D) Representative DIC images of the following strains: WT, *shf-B*, and *shf-B*:SHF-A. Scale bar: 5 μm.

consists of TOG2, a flexible central linker, and TOG3. The *C. reinhardtii* Crescerin1 homologue contains a TOG2 domain at the N-terminus followed by a central linker, TOG3, and TOG4 at the C-terminal end. The Crescerin2 subfamily, which is exclusive to vertebrates, contains only TOG3 and TOG4 domains. Given that the crystal structure of the Crescerin1 TOG2 domain has been solved and is the best characterized, we compared the *C. reinhardtii* TOG2 domain to the *Mus musculus* (mouse) TOG2 domain (Figure 2B). TOG domains contain six conserved HEAT (Huntington, elongation factor 2, phosphatase A2, TOR PI-3 kinase) that are adjacently aligned (Al-Bassam *et al.*, 2007; Slep and Vale, 2007). Each HEAT repeat is composed of two alpha helices connected by a loop. These intra-HEAT loops comprise the most conserved surface of the domain and are most similar in composition and structure to the tubulin-binding intra-HEAT loops found in ch-TOG and CLASP protein family TOG domain structures (Al-Bassam and Chang, 2011; Das *et al.*, 2015). The *C. reinhardtii* TOG2 domain contained all of these features, including a sequence predicted to form a beta-sheet hairpin that is thought to promote domain stability, specific to TOG domains belonging to the Crescerin family (Figure 2B). In addition, the *C. reinhardtii* TOG2 domain contains conserved residues at amino acid positions for which mutation variants that lead to ciliopathies, such as JBS, have been identified (Figure 2B). These similarities reaffirm that the gene mutated in the *shf-A* strain is a bona fide Crescerin1 homologue. The facts that *C. reinhardtii* has only one Crescerin1 homologue (compared with other protists that contain multiple copies) and does not contain Crescerin2 (vertebrate-specific) creates an opportunity for studying the role of Crescerin1 in flagellar regeneration and length control.

To verify whether this genetic mutation was actually causing the *shf* phenotype, we complemented the *shf-B* mutation with a *C. reinhardtii* Crescerin transgene. This transgene included the endogenous promoter, 5′UTR and 3′UTR, with a 3x-FLAG epitope tag positioned after aspartic acid 1169 to permit confirmation of transgene expression (Figure 3A). In an effort to minimize the impact of potential disruption to the secondary structure of the protein when introducing these epitopes, we selected the position for inserting these epitopes with the following criteria: 1) The region is predicted to be in an unstructured, disordered region between TOG3 and TOG4 and 2) the regions flanking the epitope contain intrinsic flexible linkers (GGS or GGA) (Chen *et al.*, 2013). When *shf-B* mutants were transformed with this transgene, cells expressing the FLAG epitope, detected through immunoblots (Figure 3B), were found to rescue the flagellar length phenotype (Figure 3, C and D), thereby confirming that the Crescerin gene mutation was indeed responsible for the *shf* phenotype.

Crescerin is encoded by the SHF1 gene of *Chlamydomonas*

We noticed that the Crescerin gene that we identified was in the same region of the genetic map (Figure 4A) as a previously described gene, SHF1, in which mutations also cause a short but non-paralyzed flagella phenotype (Jarvik *et al.*, 1984). *shf1* has long been of interest because it has several features that are unlike those of many other short-flagellar mutants. First, its length distribution shows an average length roughly half that of WT cells with a variance similar to that of WT. Second, its flagellar motility appeared normal and the cells displayed normal phototaxis, unlike many other *shf* mutants that are paralyzed. Kuchka and Jarvik (1987) had mapped the responsible gene to chromosome VI, approximately five map units from the centromere. However, the SHF1 gene was not cloned, and its identity has remained unknown. Given its location, we hypothesized that SHF1, which was the first short-flagellar gene to be genetically characterized, was in fact the gene encoding Crescerin1. To test this, we obtained *shf1-253*, *shf1-277*, and *shf1-236* from the Chlamydomonas Resource Center and confirmed that

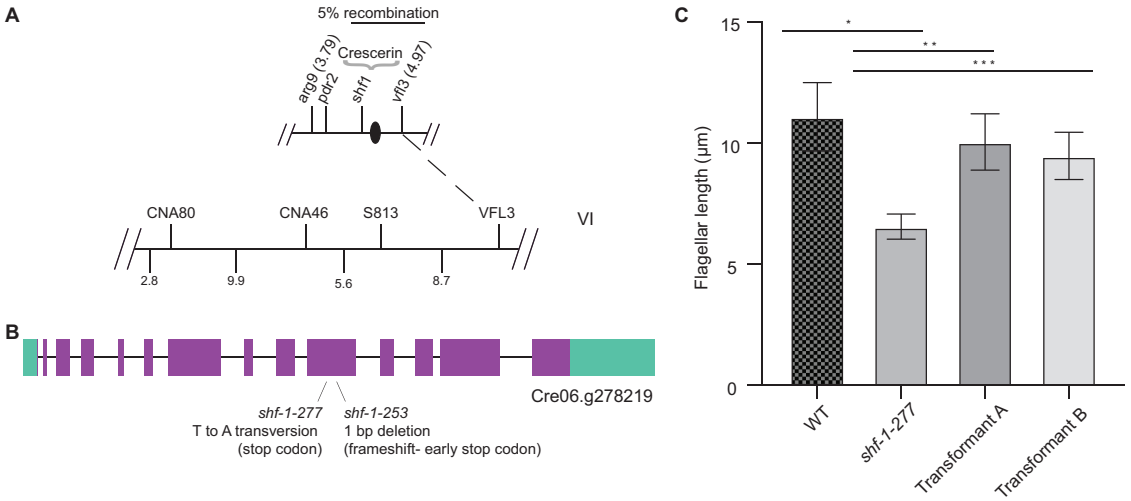

FIGURE 4: The previously identified SHF1 gene is encoded by Crescerin/Cre06.g278219. (A) Genetic map position of the SHF1 gene. The genetic map of linkage group VI (redrawn from Kathir *et al.*, 2003) is shown at the top, with the centromere represented by the black oval. The scale bar showing the percentage of recombination is above the genetic map. The starting base pair position (million) for genetic markers *arg9* and *vfl3* is indicated in parenthesis. The predicted relative location of the Crescerin gene is indicated. For reference, the Crescerin gene begins at position 4.08 (million) of chromosome 6. The molecular map is shown at the bottom, with the vertical lines indicating centimorgans; it is estimated that one centimorgan is equivalent to ~100,000 base pairs. The dashed line connecting the genetic and molecular map indicates a molecular marker corresponding directly to a previously mapped phenotypic marker. (B) The full Cre06.g278219 gene with exons in rectangles and introns as the connecting lines. Both the *shf1-277* and *shf1-253* alleles are indicated. (C) The mean flagellar lengths of WT, *shf1-277*, and two rescue strains (transformant A and transformant B) selected for their WT-like length after transformation with the SHF-C genetic construct. An unpaired *t* test was conducted for the following pairs, * *shf1-277* and WT $p < 0.0001$, ** *shf1-277* and transformant A $p < 0.0001$, *** *shf1-277* and transformant B $p < 0.0001$.

they still had the *shf* phenotype (Supplemental Figure 2A). We performed one pooled whole-genome-sequencing experiment whereby a single library was created that contained different ratios of each genome: 65% *shf1-277*, 30% *shf1-253*, and 5% *shf1-236*. This was a biased approach because we planned to align all reads only to Cre06.g278219 and analyze the allele frequencies. Our results showed that chromosome 6, position 4,096,355, contained a T-A transversion at 74% frequency and chromosome 6, position 4,096,059, contained a base pair deletion that accounted for 28% of the aligned reads. Both variants reside in exon 10 of Cre06.g278219, and both lead directly or indirectly (frame-shift mutation leading to an early stop codon), respectively, to a nonsense mutation (Figure 4B). We infer that the short-flagellar phenotype in *shf1-277* is due to the T-A nonsense mutation and in *shf1-253* is due to the single base deletion, because the approximate input of each genome in the sequenced pool, 65 and 30%, roughly parallels the observed allele frequencies, 74 and 28%, respectively. The discrepancy in the ratios is due to the sensitivity and accuracy of the DNA concentration readings and possibly DNA degradation. Because the DNA input for *shf1-236* was too low and within the range of noise, the sequence for this allele was not determined. Upon transformation with an SHF-C transgene (see Figure 3A for a description of each transgene), we found transformants that were capable of rescuing the mutant phenotype in *shf1-277* (Figure 4C and Supplemental Figure 2B). This experiment allowed us to identify the causative alleles of *shf1*. From here on, we will refer to this gene and its product as Crescerin/SHF1.

Dynamics of flagellar regeneration in SHF1

Interestingly, the original *shf1* mutant (Kuchka and Jarvik, 1987) reportedly regenerated flagella with initial kinetics similar to those of WT, but the flagellar length plateaued at a shorter value. This was in contrast to many other *shf* mutants that regenerate more slowly. We replicated this experimental result using pH shock–induced deflagellation of WT, *shf-B*, and the rescue strain (*shf-B*:SHF-A) (Figure 5A and Supplemental Figure 3A), as well as the original *shf1* mutant allele, *shf1-253* (Supplemental Figure 3B). Our results confirmed the previous results from Kuchka and Jarvik (1987) on the original *shf1* mutant and demonstrate that Crescerin/SHF1 is not required for initiation of regeneration or for the earliest stages of regrowth but becomes functionally necessary only when the flagellum reaches approximately half length to complete the structure.

Synthesis of precursor molecules is not necessary for early stages of growth but is known to be required for flagellar regeneration to full length. Genes encoding flagellar proteins are synchronously upregulated, and protein synthesis pathways are activated upon flagellar detachment (Keller *et al.*, 1984; Lefebvre and Rosenbaum, 1986; Stolc *et al.*, 2005; Yuan *et al.*, 2012). When new protein synthesis is blocked through the use of cycloheximide, flagella regenerate with initially normal kinetics but reach a shorter final length (Rosenbaum *et al.*, 1969; Lefebvre *et al.*, 1978). Typically, the length to which flagella grow in cycloheximide is referred to as the "precursor pool size," interpreted as the amount of preexisting precursor molecules that the cell body has in storage at any given moment that can be used to reassemble new flagella. Conversely, because this "pool size" (~6 µm) is ~50–60% of the average length of flagella (10–12 µm), the remaining amount of precursor molecules needed to grow the other half of the flagellum must be actively synthesized during regeneration to complete a full-length flagellum. If the size of the flagellar precursor pool were proportionally reduced in *shf1*, the a priori expectation is that cells would regenerate flagella to ~50–60% of their original length, which, given the shorter

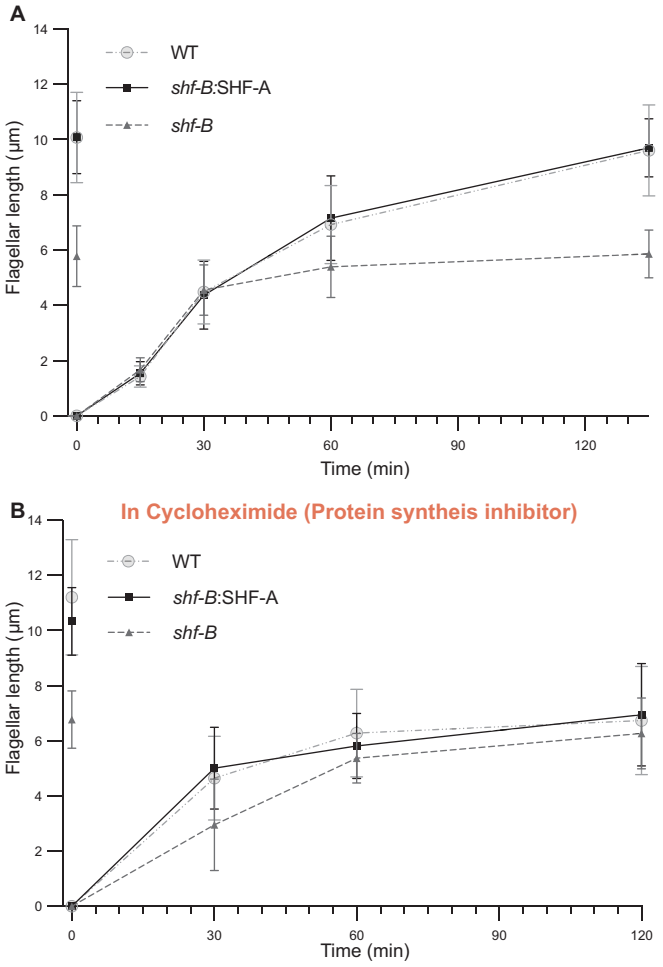

FIGURE 5: The *shf-B* mutant regenerates with early kinetics similar to those of WT and has a precursor pool size similar to that of WT. pH shock–induced flagellar length regeneration curves for cells grown in TAP media (A) and in the presence of cycloheximide (B) are shown for WT, *shf-B*, and *shf-B*:SHF-A strains. Predeflagellation lengths are shown before the 0 min time mark. The mean and error bars depicting the SD are plotted. *n* was at least 49 for each time point, strain, and treatment plotted.

initial length in the mutant, would be ~3–3.5 μm, in cycloheximide drug treatment. Kuchka and Jarvik (1987) reported that contrary to this prediction, *shf1* mutants could only regenerate short flagellar stumps in cycloheximide. In contrast to these previous claims for *shf1*, our results show that *shf-B* is in fact capable of growing back its flagella to ~92% of their original length (final average length in cycloheximide of 6.2 μm/predeflagellation average length of 6.7 μm). Therefore, the precursor pool size as defined by these experiments is seemingly unaffected compared with WT and the rescue strain as exhibited by their final average length of 6.9 and 6.7 μm, respectively (Figure 5B and Supplemental Figure 3C). We also tested the original *shf1* allele, *shf1-253*, and found that it was also capable of growing back to ~90% of its original length (final average length in cycloheximide of 5.4 μm/predeflagellation average length of 6.0 μm) (Supplemental Figure 3B). We note that one other short-flagellar mutant, *ift56-2*, has been reported to grow back to its original *shf* length in the presence of cycloheximide (Jiang, 2017), which further argues that a fixed scaling factor, between the length of flagella before deflagellation and the precursor pool size, may not exist. We hypothesize that in our *shf* mutants, the transcription and protein synthesis pathways are up-regulated normally due to the unaltered early regeneration rates, which allows for replenishing of the precursor pool to the same extent as WT cells. Supporting this hypothesis, it has been shown that the flagellar transcriptional response following deflagellation was unaffected in the shf1 allele, *shf1-253* (Kannegaard *et al*., 2014).

Dynamic relocalization of SHF1/Crescerin during flagellar regeneration

To better understand Crescerin/SHF1's role in flagellar growth and length maintenance, we determined its localization in steady state versus during regeneration. Our initial attempt was to visualize Crescerin/SHF1 directly by integrating a modified transgene containing a fluorescent protein (mCherry and green fluorescent protein [GFP]) within the Crescerin/SHF1 protein (Figure 3A); however, we were unable to detect any signal despite successful integration and complementation (Figure 4C and Supplemental Figure 2B). As an alternative approach, we immunostained *shf1* mutant strains complemented with HA-Crescerin/SHF1 using antibodies against HA and α-tubulin, at steady state and during regeneration (30 and 60 min postdeflagellation). In each condition, we observed pronounced puncta of HA-Crescerin/SHF1 within the cell body, at the base of the flagella and within the flagella, in addition to a more diffuse cytoplasmic localization (Figure 6A and Supplemental Figure 5A). The punctate localization, which has previously been reported in *C. elegans* (Das *et al*., 2015), strongly resembles IFT puncta detected through immunofluorescence of *C. reinhardtii*, suggesting a potential coupling of Crescerin/SHF1 to IFT (Wood *et al*., 2012; Ishikawa *et al*., 2014).

To quantify the signal within the flagella, we determined the intensity values for each channel by taking linescans of flagella, performing background subtraction and then normalizing the flagellar intensity of HA-Crescerin/SHF1 to tubulin. We found that the mean intensity of HA-Crescerin/SHF1 (normalized to tubulin, HA:TUB) per unit length was positively correlated with flagellar length in steady state (steady state, $R^2 = 0.77$) and late regeneration (60 min regenerating, $R^2 = 0.74$), but even more strongly correlated at midregeneration (30 min regenerating, $R^2 = 0.94$) (Figure 6B). This is in line with the idea that Crescerin/SHF1 acts as a positive regulator of flagellar length, particularly during regeneration.

To test whether the Crescerin puncta differentially localizes during regeneration compared with at steady state, we performed puncta detection for flagella in all three conditions. We found that puncta showed a bias toward being localized at the tip of the flagella in steady-state cells and both at or near the tip for 30-min-regenerating flagella (Figure 6C) but not for 60-min-regenerating flagella, in line with previous accounts on Crescerin/SHF1 localization (Louka *et al*., 2018). Interestingly, puncta were detected very early on during regeneration in short flagella, which decreases the likelihood that Crescerin/SHF1 import is triggered at a set length during regeneration. In all three conditions there was no particular flagellar length for which puncta were most enriched, suggesting that Crescerin/SHF1 is not exclusive to any particular length (Supplemental Figure 5B). The number of puncta per micrometer of flagella increased slightly at 30 min of regeneration compared with 60 min of regeneration and steady-state cells (Supplemental Figure 5C), which prompted us to analyze the number of puncta per micrometer of flagella as a function of flagellar length. Overall, the trend is that as flagella get longer during regeneration, the number of puncta per micrometer seems to decrease, which is an observation that mirrors the distribution of IFT trains (Figure 6D) (Engel *et al*., 2009; Craft *et al*., 2015; Ludington *et al*., 2015).

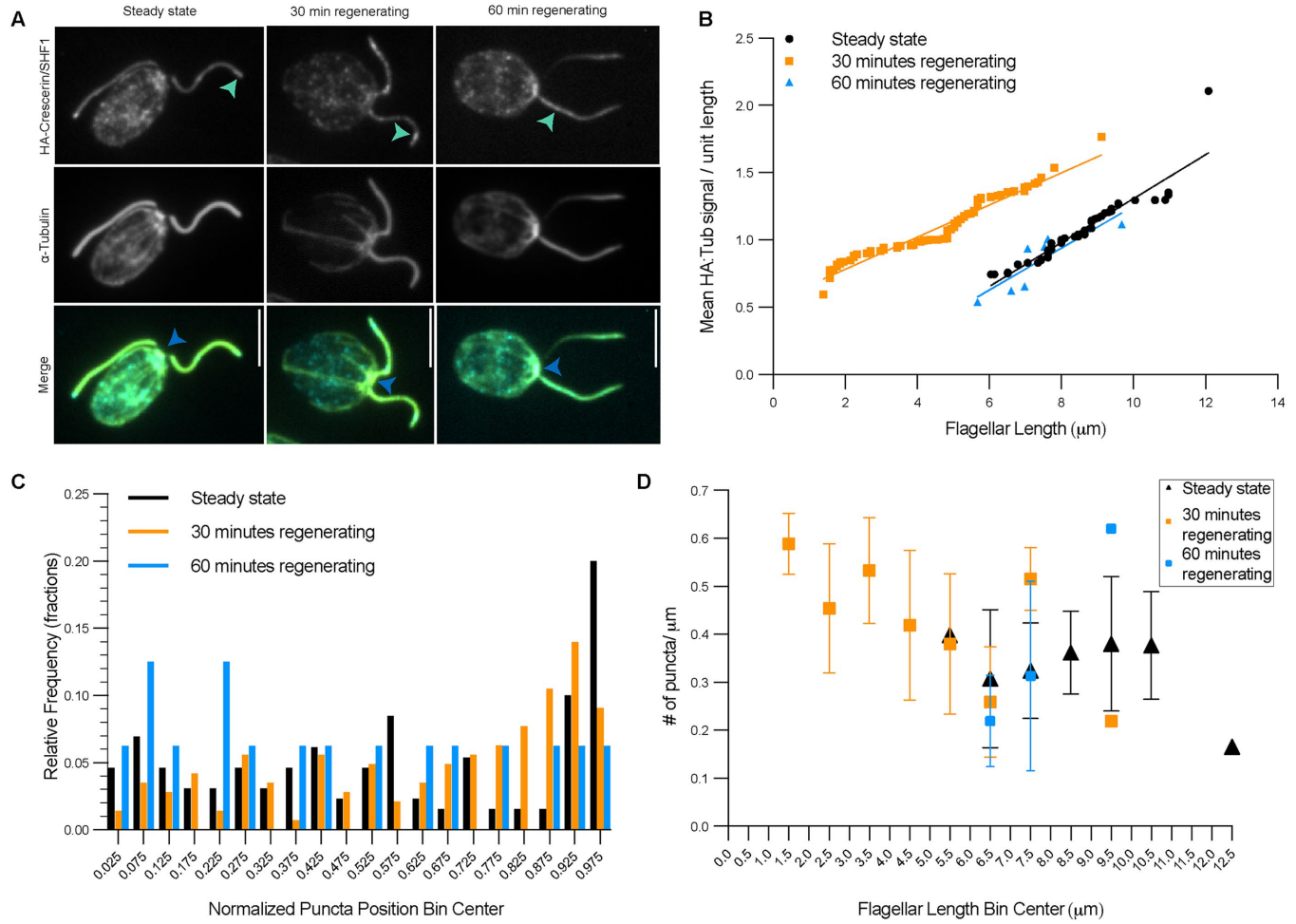

FIGURE 6: Localization of HA-Crescerin/SHF1 and tubulin within flagella during regeneration. (A) Mutant strains complemented with HA-Crescerin/SHF1 were fixed at steady state (predeflagellation) or during regeneration at 30 or 60-min post-pH shock, immunostained against HA-Crescerin/SHF1 and α-tubulin, and displayed as a sum-slices Z-projection. The light green arrowheads show examples of puncta within the flagella, whereas the blue arrowheads show accumulation of HA-Crescerin/SHF1 at the base of the flagella. (B–D) Intensity line scans for each channel were taken from flagellar base to tip. Puncta were identified by thresholds described in *Materials and Methods*. (B) Scatter plot of mean HA:TUB intensity per unit length vs. length of each flagellum (one data point is one flagellum). Steady state: 47 flagella, 30 min regenerating: 78 flagella, 60 min regenerating: 7 flagella. (C) Relative frequency distribution plot of the location of all puncta within the flagella that were identified in steady-state flagella and flagella regenerating for 30 and 60 min. Puncta location is normalized to the measured flagellar length. Steady state: 130 puncta, 30 min regenerating: 143 puncta, 60 min regenerating: 16 puncta. The bin size is 0.05. (D) The mean and SD of the number (#) of puncta per micrometer of flagella were plotted against the measured flagellar length for steady-state flagella and flagella regenerating for 30 and 60 min. The bin size is 1 μm. Scale bar: 5 μm.

Modeling Crescerin/SHF1 function in flagellar assembly

The results thus far establish that Crescerin/SHF1 is necessary for achieving normal flagellar length in *C. reinhardtii*. Given that Crescerin/SHF1 contains several putative microtubule-binding TOG domains, which are known to bind tubulin and to help facilitate microtubule polymerization, and given that Crescerin/SHF1 appears to be associated with both IFT trains and the flagellar tip (Bacaj *et al.*, 2008; Das *et al.*, 2015; Louka *et al.*, 2018), there are at least two potential ways that Crescerin/SHF1 may contribute to length regulation. In one model (Figure 7A), Crescerin/SHF1 acts as a microtubule polymerase at the flagellar tip, facilitating the incorporation of tubulin dimers onto the end of the growing outer doublet microtubules. An alternative model is that Crescerin/SHF1 may help to bind tubulin dimers in the cytoplasm and transport them into the flagellum (Figure 7B). Are both of these models equally able to explain the *shf1* phenotype? We implemented a computational model (see *Materials and Methods*) that represents the processes of tubulin import, flagellar microtubule turnover, and cytoplasmic microtubule dynamics. Using this model, we asked which of the two scenarios, microtubule polymerization or tubulin transport, can best explain the observed mutant phenotype, which we characterize in terms of three features: 1) a steady-state flagellar length that is roughly half that of WT cells, 2) no observable difference in flagellar growth rate between mutant and WT during the initial phase of growth up to several micrometers, and 3) during regeneration in the absence of protein synthesis, WT flagella grow back to roughly half their preshock length while mutant flagella grow back to ~80% of preshock length. Given the highly simplified nature of our computational model, we do not expect precise numerical matching of experimental data. Rather we ask whether the simplified model can or cannot

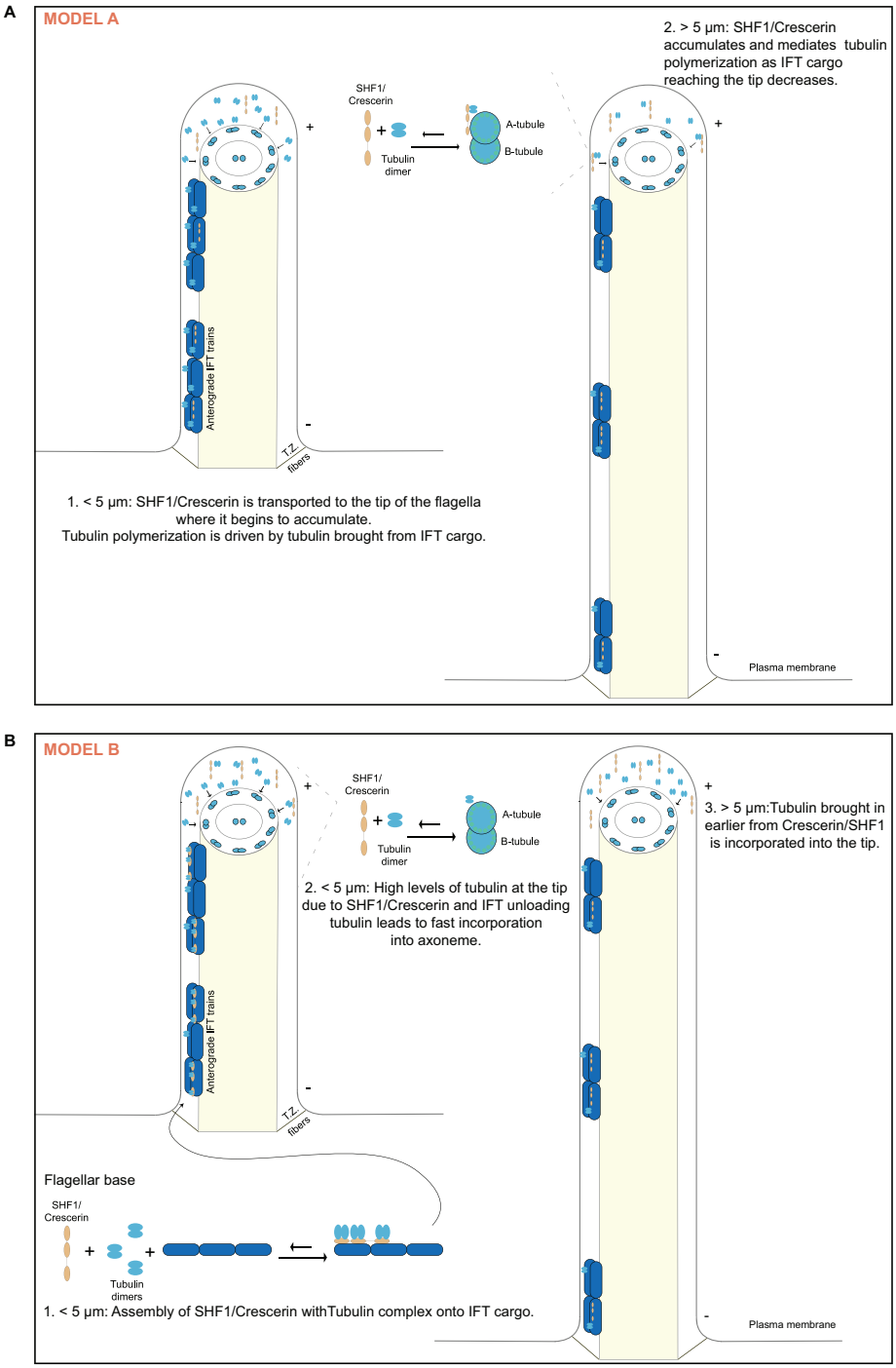

FIGURE 7: Two hypothesized mechanisms for how Crescerin/SHF1 could regulate flagellar length. (A) Microtubule polymerase model. In the early stages of regeneration, flagella have anterograde IFT trains that are large in size and frequently reach the tip. This would lead to a readily available tubulin pool at the tip of the flagella. As flagellar regeneration continues, IFT train size decreases, as does the frequency of trains reaching the plus ends. If the tubulin concentration dips below the critical concentration for self-polymerization, Crescerin/SHF1 would become crucial for accelerating polymerization and decreasing the effective tubulin concentration necessary for polymerization. (B) Tubulin-binding-site model. In the early stages of regeneration, the TOG domains of Crescerin/SHF1 bind to tubulin and load onto the IFT trains. This Crescerin/SHF1 + tubulin cargo would increase the amount of tubulin inside the flagellum compared with what could be imported if IFT molecules were the sole tubulin-binding components. During early stages of growth, the axonemal growth rate is at its maximum because the amount of tubulin reaching the tip is in excess. In this model, Crescerin/SHF1 acts preemptively by substantially increasing the concentration of tubulin at the tip to allow for growth at later stages when IFT trains reaching the tip start to decline.

replicate the three qualitative aspects of the phenotype.

As seen in Figure 8A, a model based on loss of an elongation factor at the tip does not account for the observed phenotypes. It can explain the reduced steady-state length in the mutant, but in such a model, it is predicted that flagella regenerated in cycloheximide should be extremely short, or not regenerate at all. This is consistent with prior reports from Kuchka and Jarvik (1987) but is not consistent with our observations (Figure 5B and Supplemental Figure 3B). The polymerase model also predicts a much slower initial growth rate, which again is not consistent with our observations. In contrast, a model based on loss of high-affinity tubulin-binding domains from the IFT particle, corresponding to the TOG domains of Crescerin/SHF1 (Figure 8B), is able to recapitulate the observation that flagella regenerate to a length closer to preshock length in cycloheximide-treated mutants than in cycloheximide-treated WT cells (Figure 5B and Supplemental Figure 3C).

Figure 8A shows the result of simulations using one specific set of model parameters, but as discussed in *Materials and Methods*, systematic variation of model parameters was unable to identify a parameter set in which a reduction in polymerization rate resulting in half-length flagella at steady state could also allow flagella to regrow after deflagellation in the absence of new protein synthesis. One particular combination of parameters that we explored was reduced elongation rate (as per the polymerase model tested in Figure 8A) along with reduced tubulin binding by IFT (as per the tubulin-loading model of Figure 8B). This type of model would represent a situation in which Crescerin plays roles in both tubulin binding/import as well as tubulin polymerization at the flagellar tip. Figure 8C illustrates simulation results for four different levels of tubulin binding ranging between the fully mutant and fully WT examples plotted in Figure 8B. For each set of tubulin-binding parameters, we then varied the elongation rate constant to simulate mutations that reduce polymerase activity in addition to the reduced tubulin binding. As can be seen in Figure 8C, reducing the elongation rate always has a much more severe effect on the length of flagella regenerated in the absence of protein synthesis, compared with the effect that it has on the preshock flagellar length. The only combination of parameters that reflects our observations is when the Crescerin mutant affects tubulin binding but has minimal effect on elongation rate.

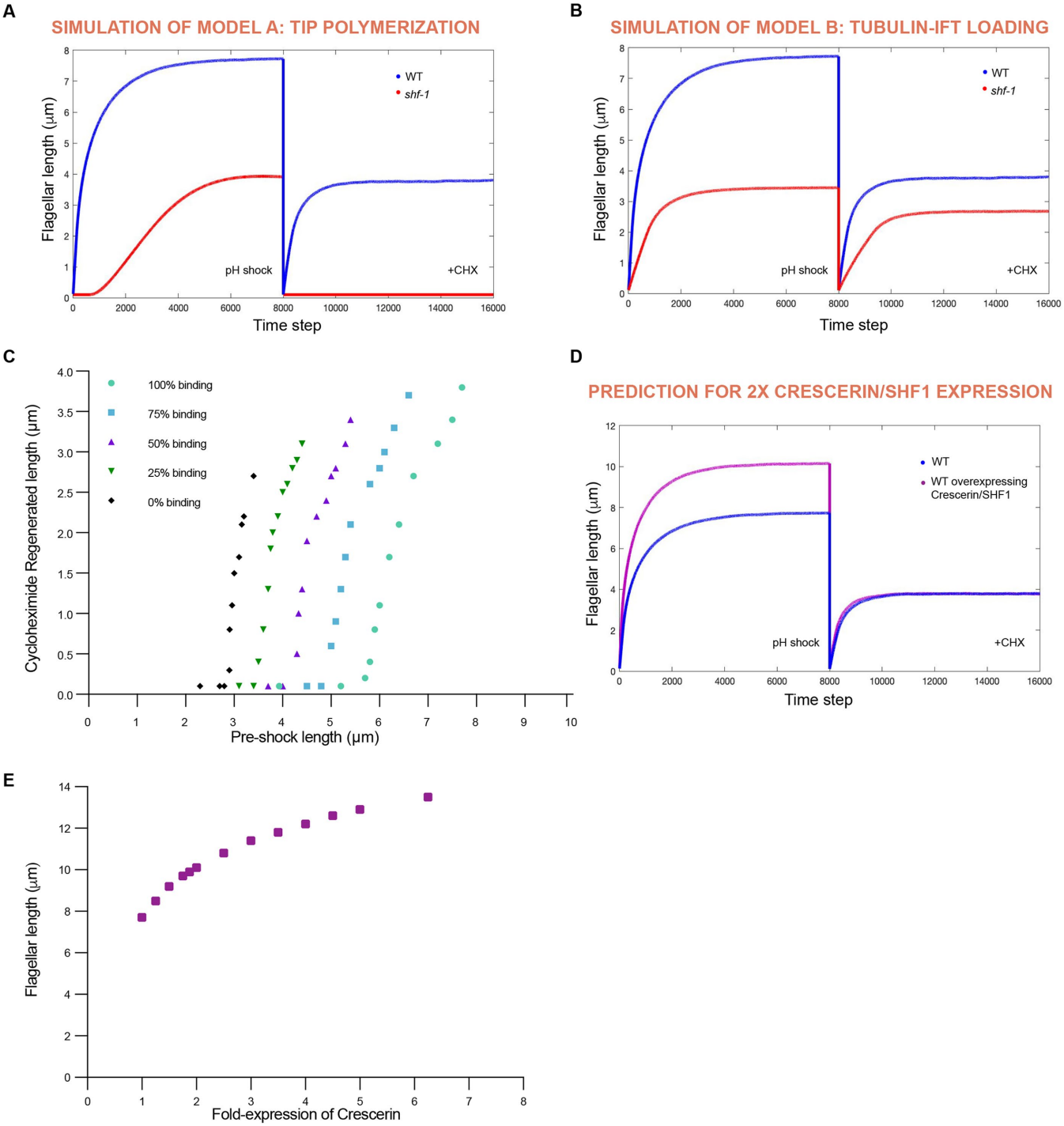

FIGURE 8: Computer simulations of regeneration kinetics in the *shf1* mutant (A, B) Simulations in which the flagellum is allowed to grow out from zero length until it reaches steady state (left on the graph) and then the flagellum is removed once more and allowed to regrow without increasing the cytoplasmic pool (right on the graph). The second regrowth phase is analogous to the cycloheximide experiment (+CHX) because it uses the pool of unassembled components in the cell body that remained after the recent flagellar assembly. (A) Simulation in which the *shf1* mutant affects polymerization rates as in model A of Figure 7. The sole parameter that changed between WT and *shf1* is the elongation rate of the microtubule as a function of tubulin concentration inside the flagella. In this scenario, the flagellar length of the *shf1* mutant showed an approximately two-fold decrease compared with WT (left side) that was observed in our experiments; however, it was incapable of regrowing in the +CHX simulation (right side). (B) Simulation in which the *shf1* mutant affects tubulin binding as in model B of Figure 7. Two parameters were altered to allow for the differences between WT and the *shf1* mutant. First, the dissociation constant of the IFT particles for capturing tubulin was increased two-fold in the mutant. Second, the constant describing the number of IFT particles and effective cargo-carrying capacity was decreased two-fold in the mutant. In this scenario, the flagellar length difference between WT and the *shf1* mutant reflects the experimental values (left side) and the +CHX simulation shows that the *shf1* mutant

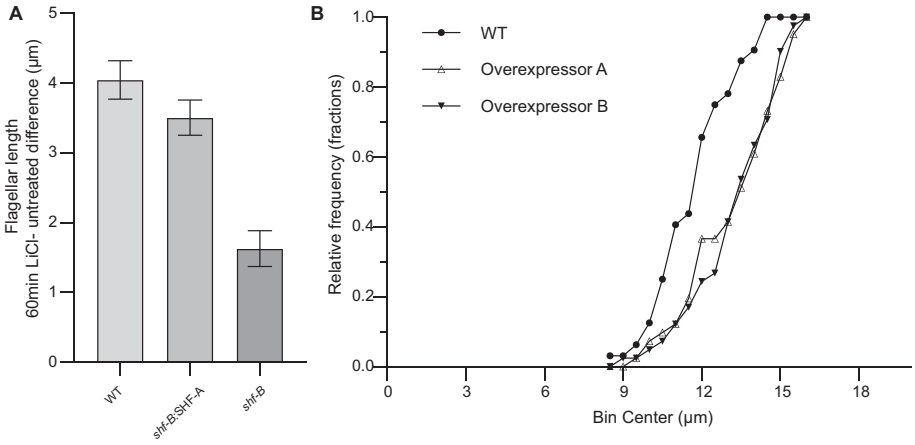

FIGURE 9: Relation between Crescerin/SHF1 and flagellar length. (A) Crescerin/SHF1 is important for growth from longer lengths. The flagellar length mean difference between cells grown for 60 min in the presence of LiCl and untreated cells is shown for WT, *shf-B*:SHF-A, and *shf-B*. The error bars are the SE for the difference between the two means. (B) Increased Crescerin/SHF1 expression leads to increased length. Steady-state flagella of WT (CC-5325) cells ($n = 32$) and WT cells expressing the SHF-B construct, overexpressor A ($n = 41$) and overexpressor B ($n = 41$), were measured and plotted as a cumulative frequency graph. A Kolmogorov–Smirnov test was performed between the following pairs: WT and overexpressor A ($p = 0.0055$); WT and overexpressor B ($p = 0.0005$).

If we increase the quantity of Crescerin/SHF1 in the model, such as could be achieved by overexpression, a longer steady-state length is predicted (Figure 8D). However, the relationship between Crescerin/SHF1 levels and steady-state length is nonlinear, such that a sixfold increase in Crescerin/SHF1 would be required to produce a doubling of length (Figure 8E). Thus, our model makes the prediction that Crescerin/SHF1 overexpression should lead to a measurable length increase, but even with a strongly expressing construct, less than an overall doubling of length.

Effect of Crescerin/SHF1 on steady-state length

The fact that *shf1* mutant cells stop growing flagella at approximately half WT length without having exhausted the precursor pool suggests that the mutant flagella are unable to make full use of the existing pool at this length. We therefore asked how the absence of Crescerin/SHF1 would affect the growth of flagella starting at steady-state length when their elongation is stimulated. In *C. reinhardtii*, incubation of cells with lithium chloride (LiCl) is used to induce flagellar growth from steady-state lengths (Nakamura *et al.*, 1987). Although the exact mechanism is not known, LiCl elongation is associated with increased IFT within the flagellum (Ludington *et al.*, 2013) and is known to occur through the recruitment of flagellar precursor proteins from the cell body pool (Wilson and Lefebvre, 2004). Our expectation was that LiCl-induced elongation would be impaired in the *shf-B* mutant possibly due to decreased capacity for tubulin transportation. We found that upon 60 min of LiCl treatment, WT and the rescue line increased their lengths by an average of 4 and 3.5 µm, respectively, but *shf-B* mutant cells increased flagellar length by only 1.6 µm (Figure 9A and Supplemental Figure 4A). We note that while these results are consistent with a decrease in tubulin import, they do not disprove the polymerase model because a loss of polymerization activity in the *shf-B* mutant would also potentially be consistent with the same result.

One prediction of the tubulin import model is that increased levels of Crescerin/SHF1 would increase the steady-state flagellar length (Figure 8, D and E). This result was first reported in hTERT-RPE1 cells, where overexpression of Crescerin/SHF1 was shown to increase cilia length (Latour *et al.*, 2020). To test this prediction in *Chlamydomonas*, we introduced a Crescerin/SHF1 transgene in WT cells. Cumulative frequency plots show that transformants overexpressing Crescerin/SHF1 had increased flagellum length distribution compared with unaltered WT cells (Figure 9B and Supplemental Figure 4, B and C). This effect suggests that one possible method for regulating the steady-state length of the flagellum is to tune the levels of Crescerin/SHF1.

DISCUSSION

The role of Crescerin in flagellar elongation

Within the context of the balance point family of models, there are four ways to make a shorter flagellum: reduction of IFT, reduction of precursor pool synthesis, increased disassembly of the axoneme, and reduced incorporation of tubulin from the precursor pool into the flagellum. Given that the early rapid phase of regeneration is primarily driven by IFT and the *shf1* mutant is unaffected in this growth phase up to half length, it is improbable that IFT rates are grossly affected in the *shf1* mutant. Furthermore, the ability of *shf1* mutants to elongate in response to LiCl suggests that IFT is still functioning properly at steady state, in contrast with the actin mutant, *ida5*, which is completely incapable of flagellar elongation upon LiCl treatment due to an impairment of actin-dependent IFT recruitment to the basal bodies and/or train size regulation (Avasthi *et al.*, 2014).

is capable of regenerating to ~78% of its predeflagellation length (right side), which is similar to the experimental results shown in Figure 5B and Supplemental Figure 3B. (C) Simulation combining effects on both polymerization rate and tubulin binding. Five different values for tubulin binding, ranging from the WT rate (blue curve of panel B) to fully mutant (red curve of panel B) were combined with a range of elongation rates. Colored symbols represent the different values of tubulin binding. Plot shows the preshock steady-state length on the *X* axis and the length of flagella regenerated in cycloheximide on the *Y* axis. The high slope of the curves indicates that reduction of polymerase rate has a stronger effect on the cycloheximide-regenerated length than on the preshock steady-state length. (D) Simulation of Crescerin overexpression assuming the tubulin-binding model. This model simulates the regeneration curve of WT and a strain that has twofold overexpression of Crescerin/SHF1. In this simulation, the constant describing the number of IFT particles and effective cargo-carrying capacity was increased twofold relative to WT. (E) Predicted effect of Crescerin overexpression. The figure plots the steady-state length vs. relative Crescerin levels, where a relative level of 1 corresponds to a WT cell, indicating that while increased Crescerin expression should lead to increased length, the length increase is nonlinear with respect to the level of overexpression.

The fact that *shf1* mutant flagella grow back almost to the pre-deflagellation length in cycloheximide (Figure 5B and Supplemental Figure 3B), together with prior results that flagellar genes are fully induced during regeneration in an *shf1* mutant (Kannegaard *et al.*, 2014), argues against the possibility that growth in *shf1* mutants is impaired due to a defect in precursor pool synthesis. Our results taken together are most consistent with the idea that in the *shf1* mutant, tubulin incorporation into the axoneme at the distal tip is decreased, although not abolished, due to a role of Crescerin/SHF1 protein in tubulin transport or dynamics.

Tubulin and Crescerin/SHF1 in flagellar length control models

Because tubulin represents the most abundant, main structural unit of the axoneme, large quantities of tubulin need to move from the cell body to the tip of an assembling flagellum. One question that has been largely explored is how to reconcile the observed kinetics of flagellar assembly with the rate at which tubulin reaches the flagellar tip (Bhogaraju *et al.*, 2014).

Bhogaraju and colleagues hypothesized that aside from the tubulin-cargo–binding site they had discovered, several other tubulin-cargo–binding sites in IFT proteins may exist to compensate for the decreased tubulin amounts as assembly proceeds (Bhogaraju *et al.*, 2014). Our results suggest an alternative: increased tubulin recruitment is provided by the tubulin-binding TOG domains of Crescerin/SHF1. Our immunofluorescence experiments show Crescerin/SHF1 in puncta at the distal region and along the flagella from the commencement of regeneration, suggesting that Crescerin/SHF1 is trafficked by the IFT system. Corroborating this idea are previous findings showing that the Crescerin/SHF1 homologue in *C. elegans*, CHE-12, requires IFT particle B to localize to the flagella (Bacaj *et al.*, 2008). Furthermore, CHE-12 GFP puncta were detected showing anterograde and retrograde movement in the flagella (Das, 2016). Most recently, tandem affinity purification combined with mass spectrometry of Crescerin/TOGARAM1 identified multiple IFT-B proteins as possible binding partners (Latour *et al.*, 2020). Our results indicate that Crescerin is associated with IFT particles at the earliest stages of flagellar assembly, even though the flagellar regeneration curve indicates that loss of Crescerin/SHF1 is felt only when the flagellum reaches a certain length. In our computational model, Crescerin allowed IFT particles to import tubulin at a rate that exceeded the growth rate of the flagellum, allowing the flagellum to transiently build up a reserve of tubulin that was then used to allow for assembly when the frequency of IFT cargo deposits at the tip decreases later in regeneration.

During assembly, the tubulin concentration at the tip is predicted to decrease in part due to IFT trains decreasing in size and injection rates decreasing as a function of ciliary length (Marshall and Rosenbaum, 2001; Marshall *et al.*, 2005; Engel *et al.*, 2009; Ludington *et al.*, 2013). Even though tubulin can reach the tip of an assembling flagellum through diffusion, IFT is necessary to promote the proper concentration for assembly of tubules at the tip (Craft Van De Weghe *et al.*, 2020). In fact, when a tubulin-binding motif on the IFT cargo molecules is mutated, flagellar regeneration and length are impaired significantly (Bhogaraju *et al.*, 2013b; Kubo *et al.*, 2016). Our modeling work found that it was necessary to change two parameters in order to account for the ability of *shf1* mutants to regenerate to within 90% of their preshock length in cycloheximide. Specifically, this effect was seen only when the number of tubulin-binding sites per IFT particle decreases and the affinity of the remaining sites for tubulin decreases, compared with WT. These two parameter changes would be achieved in an *shf1* mutant if Crescerin/SHF1 is associated with IFT particles, where it provides tubulin-binding sites of high affinity relative to the non- Crescerin tubulin-binding sites of the core IFT proteins. Future biochemical characterization of Crescerin/SHF1 are required to prove that this protein does in fact act as a tubulin-binding factor for the IFT system. Regulation of Crescerin/SHF1 activity could provide a regulatory point that would affect tubulin loading onto IFT, as is the case with the structural protein DRC-4 (Wren *et al.*, 2013). Proteomic data of *C. reinhardtii* cells have identified multiple phosphorylated and oxidized residues in the disordered regions between the TOG domains and within TOG-3 (Wang *et al.*, 2014; Ford *et al.*, 2020). One intriguing possibility is that these residues get modified by kinases to tune the affinity of Crescerin/SHF1 to tubulin and IFT molecules. Many kinases have been found to play a role in flagellar length control, but almost nothing is known about their physiologically relevant substrates (Berman *et al.*, 2003; Pan *et al.*, 2004; Wilson and Lefebvre, 2004; Bradley and Quarmby, 2005; Tam *et al.*, 2007, 2013; Luo *et al.*, 2011). We propose that some of these length-regulating kinases may work via an effect on Crescerin.

Another important factor affecting the ability to form IFT–tubulin cargoes is the soluble tubulin concentration at the base of the flagella, which in turn depends on the cytoskeleton microtubule dynamics in the cell body. In *C. reinhardtii*, katanin, a cytoplasmic microtubule-severing protein, and kinesin-13, a microtubule depolymerizer, have loss-of-function mutant phenotypes that lead to flagellar length abnormalities (Piao *et al.*, 2009; Qasim Rasi *et al.*, 2009; Wang *et al.*, 2013; Kannegaard *et al.*, 2014). These results suggest that the tubulin dynamics of the cell body affect flagellar length. This underscores the need to better understand soluble tubulin concentrations both at the tip and at cargo assembly locations near the basal bodies, because subtle changes in tubulin concentration can lead to major changes in the frequency of IFT–tubulin complex formation. Future biochemical characterization experiments determining the affinities of these interactions are necessary to gain a more detailed mechanistic understanding of these processes. Such biochemical measurements will also greatly constrain possible models for Crescerin function, allowing future computational simulations to be increasingly realistic.

TOG domains have conserved tubulin-binding features found in several well-studied protein families such as XMAP-215 and CLASP proteins (Slep and Vale, 2007; Al-Bassam *et al.*, 2010; Fox *et al.*, 2014; Byrnes and Slep, 2017). Structural analysis of a TOG domain in Crescerin/SHF1 has identified conserved key features such as the intra-HEAT loops that bind to tubulin in XMAP-215 and CLASP protein families (Das *et al.*, 2015). We also found that these features are conserved in the TOG domains of the *C. reinhardtii* homologue (Figure 2B). In vitro polymerization assays with purified mammalian Crescerin/SHF1 TOG domains have shown that each domain can additively increase tubulin polymerization (Das *et al.*, 2015). Moreover, point mutations that disrupt binding of the TOG domains to tubulin phenocopy a Crescerin/SHF1 knockout in its shorter flagellar length at steady-state, suggesting that tubulin binding is paramount for its activity. Cumulatively, these results imply that Crescerin/SHF1 is binding to tubulin and increasing polymerization; however, the latter has never been explored in vivo. In terms of the competition between cytoplasmic and flagellar microtubules, we infer that Crescerin is mainly acting on the latter, because its loss leads to shorter flagellar length. If Crescerin was acting to promote cytoplasmic microtubule polymerization, then its loss would lead to longer flagella. In terms of Crescerin's function in flagellar microtubules, our modeling simulations suggest that Crescerin/SHF1's tubulin-binding ability acts as a recruiting factor for IFT particles as they enter the flagellum rather than acting as a polymerase at the flagellar tip.

Comparison between flagellar TOG-domain proteins Crescerin/SHF1 and Cep104/Fap256

In *Tetrahymena*, another TOG-domain–containing protein, Cep104/Fap256, was reported to localize near the A-tubule, whereas Crescerin/SHF1 was found near the B-tubule, which led Louka *et al.* (2018) to suggest that each of these proteins helps assemble tubulin on each respective tubule. Among flagella there is dramatic variation in the size and composition of the distal segment defined as a region at the tip consisting of only an A-tubule singlet due to a gap between the plus ends of the longer A-tubule and shorter B-tubule. In *C. reinhardtii* and *Trypanosoma brucei*, a distinct singlet distal segment was not observed through cryoelectron tomography reconstructions at steady state (Höög *et al.*, 2014). Furthermore, during assembly of flagella, *C. reinhardtii* flagella had approximately equal lengths of A- and B-tubules (Höög *et al.*, 2014). Given that the early flagellar regeneration kinetics was nearly the same in WT as in the *shf1* mutant, we find it improbable that Crescerin/SHF1 is important only for B-tubule formation.

In *C. reinhardtii* (Satish Tammana *et al.*, 2013; Rezabkova *et al.*, 2016; Al-Jassar *et al.*, 2017), mutants in Cep104/Fap256, known as *roc22*, have shortened flagella similar to *shf1*. However, most cells (~70%) fail to regenerate flagella after pH shock–induced deflagellation (Satish Tammana *et al.*, 2013). This result suggests that unlike Crescerin/SHF1, Cep104/Fap256's function is crucial from the onset of regeneration. The distinct mutant phenotypes of *roc22* and *shf1* cells revealed in regeneration experiments indicate that these proteins have different temporal regulatory roles in flagellar assembly: Cep104/Fap256 is key for the start of assembly, and Crescerin/SHF1 is crucial during the early stages to enrich for tubulin at the tip. Interestingly, in a recent study, Cep104/Fap256 and Crescerin/SHF1 were found as part of a larger protein complex in mammalian cell lines (Latour *et al.*, 2020). Given the presence of one TOG domain in Cep104/Fap256 and three TOG domains in Crescerin/SHF1, we speculate that the two proteins in complex with each other and possibly with other MAPs can lead to altered on and off rates with tubulin compared with each individual component.

From these perspectives, it will be intriguing to decipher how these two proteins work together to regulate flagellar microtubule dynamics. In *C. reinhardtii* and *Tetrahymena* flagella, Cep104/Fap256 has been found exclusively at the tip during assembly and at steady state (Satish Tammana *et al.*, 2013; Louka *et al.*, 2018). In contrast, Crescerin/SHF1 localizes in puncta at the tip and along the flagella. Perhaps Crescerin/SHF1's extra stretches of positive residues located C-terminal to its TOG domains, shown to be important in binding to the microtubule lattice in XMAP215 and CLASP (Al-Bassam *et al.*, 2006, 2010; Brouhard *et al.*, 2008), allow for attachment modules along the lattice of the microtubules, which could increase tubule stability during steady state. Crescerin/SHF1 contains a TOG-domain architecture similar to that of the CLASP proteins. The family of CLASP proteins decrease microtubule catastrophe and promote microtubule rescue (Slep, 2018). This added functionality could also explain the increased prevalence of Crescerin/SHF1 puncta at the tip in nonassembling flagella.

MATERIALS AND METHODS

Request a protocol through *Bio-protocol*.

Initial identification of strain carrying a candidate short-flagellar mutation

We originally set out to understand how the massive transcriptional response that is turned on during flagellar regeneration ties back to flagellar length control. Publications focusing on gene expressionduring the cell cycle highlighted the expression profiles of putative transcription factors that are up-regulated following deflagellation (Albee *et al.*, 2013; Zones *et al.*, 2015). Assuming that there could be a feedback loop that turns on these transcription factors during flagellar regeneration, we hypothesized that mutations in these up-regulated transcription factors would result in flagellar length abnormalities. Therefore, we screened for changes in flagellar length in a set of insertional mutants predicted to disrupt genes encoding these putative transcription factors. Candidate genes were identified as annotated transcription factors in Zones *et al.* (2015) (summarized in sheet 1 of Supplemental_Table_1). The mutants that we screened did not have any visible length abnormalities in steady-state conditions with the exception of mutant LMJ.RY0402.093488_1, which was predicted to contain a genetic lesion in Cre01.g003376. Cre01.g003376 is predicted to encode a transcription factor with a putative Myb-like DNA-binding domain. This strain had shorter flagella (*shf*) than WT. To test whether the transcription factor disruption was causing the short-flagellar phenotype, we analyzed another mutant, LMJ.RY0402.230098, with a predicted insertion cassette (95% confidence) in the intron of the same gene, Cre01.g003376. This second mutant did not have an *shf* phenotype in steady-state conditions. Given these differences in phenotypes, we asked whether some other mutation besides the insertion at Cre01.g003376 was leading to this phenotype. Therefore, we backcrossed the mutant exhibiting the short-flagellar phenotype (LMJ.RY0402.093488_1) to WT cells to see whether the mutant phenotype cosegregated with the paromomycin cassette. Through tetrad analysis, we found thatone full paromomycin cassette was present (2:2 segregation) and that the short-flagellar phenotype segregated 2:2 and was therefore presumably due to a single mutation, but that paromomycin resistance and the short-flagellar phenotype did not cosegregate. Furthermore, a PCR designed to detect the junction site of the Cre01.g003376 locus (sheet 2 of Supplemental_Table_1) with the paromomycin cassette showed that the paromomycin resistance was indeed coming from the Cre01.g003376 locus disruption, eliminating the possibility that a full paromomycin resistance cassette inserted elsewhere in the genome was causing the short-flagellar phenotype. Thus, it became increasingly clear that the short-flagellar phenotype was not actually due to the transcription factor gene lesion we had originally chosen to screen. The mutation apparently identifies a gene involved in flagellar length control, and we denoted it initially as SHF-A, to indicate the fact that we did not initially know whether it related to any previously described short-flagellar genes.

Strains and media

Chlamydomonas strains were obtained from the Chlamydomonas stock center. WT strains include CC-125 mt+ and CC-5325 cw15 mt– (the latter is the background strain of the Chlamydomonas Library Project). The original un-backcrossed *shf-A* mutant is LMJ.RY0402.093488. *shf-A* was backcrossed twice to CC-125 mt+. *shf-B* isLMJ.RY0402.172376 and has a paromomycin resistance cassette insertion at the same location where the 5-base-pair deletion starts in *shf-A*. For the *shf1* mutants, the following strains were used: CC-2348 (*shf1-253*), CC-2347 (*shf1-277*), and CC-2345 (*shf1-236*). For liquid cultures, cells were grown either in M1 media (Sager and Granick Medium 1) in a 14:10-h light:dark cycle and measured during the light part of the cycle or in Tris-acetate phosphate (TAP) media for ~2–3 d in constant light. Cells were maintained in 1.5% TAP agar plates; however, if a strain carried a paromomycin resistance cassette, it was kept in media supplemented with 20 µg/ml paromomycin. Strains containing a Crescerin/SHF1 transgene

construct were maintained in solid media containing 20 µg/ml hygromycin.

For gamete formation, cells were restreaked onto fresh TAP agar and incubated in low light. They were then transferred onto TAP-N medium for 4–5 d to induce gametogenesis. The gametes from each strain were then resuspended using 150–200 µl of TAP until a dark green resuspension was obtained. Sporulation and dissection were done as in Perlaza *et al.* (2019).

Whole genome sequencing

Culture conditions for original mutant pooled spores. The original mutant LMJ.RY0402.093488 was backcrossed twice to CC-125 mt+ [137c]. Spores from tetrads and octads were scored for short- versus WT-length flagella. Twenty spores corresponding to each category, WT or short, were grown as follows: cultures (2 ml per well) for each spore were grown on 24-well plates in alternating dark:light cycles (14:10) for 3 d. To make sure that there was equal representation of each spore's genomes, the cell density for each spore was checked to ensure equal input before pooling. One milliliter per spore was used for each phenotypic pool for a total of 20 ml per sample, WT versus mutant. The genomic DNA (gDNA) extraction was performed as described in the pooled genome sequencing method in Perlaza *et al.* (2019).

The sequencing libraries were prepared with the aid of the KAPA hyperprep library kit by the Vincent J. Coates Genomics Sequencing Laboratory and Functional Genomics Laboratory at the University of California, Berkeley. One cycle of PCR was used to linearize the library molecules. Fragment analyzer traces and Qubit values were assessed for each sequencing library as quality control checks. Pooled 150PE NovaSeq S4 sequencing was performed at the UCSF Center for Advanced Technology Lab. Twenty gigabytes of data was requested per sample.

Culture conditions and gDNA preparation for shf1 mutants. Strains CC-2345 (*shf1-236*), CC-2347 (*shf1-277*), and CC-2348 (*shf1-253*) were streaked out to singles to ensure an isogenic population of cells. The cultures conditions and gDNA extractions were done exactly as described in *Culture conditions for original mutant pooled spores*, with the exception that the starting volume of each strain was ~7 ml. The concentrations of DNA were determined by a nanodrop. The final gDNA sample that was sent to sequence was a pooled sample that combined ~65% of *shf1-277*, ~30% of *shf1-253*, and 5% of *shf1-236* gDNA.

The gDNA pool was prepped for sequencing using the NEB Ultra II DNA library kit. Fragment analyzer traces and Qubit values were assessed for each sequencing library as quality control checks. Novaseq 6000 sequencing was performed by Novogene with 15 GB of data requested.

Processing of sequence data. Unless otherwise noted, the following steps were used for analyzing data from the WT versus mutant pooled experiment samples and the various ratios of *shf1* allele pool sample.

The raw sequences were processed using FastQC: a quality control tool for high throughput sequence data, version 0.11.8 (https://www.bioinformatics.babraham.ac.uk/projects/fastqc/). Trimmomatic was used for quality filtering of the reads and to remove sequences that match the adapter (Bolger *et al.*, 2014). These reads were then aligned to version 5.0 of the *C. reinhardtii* genome DOE Joint Genome Institute (JGI), reference strain CC-503, mt+ (Merchant *et al.*, 2007) using the Burrows-Wheeler Aligner (BWA) (Li and Durbin, 2009). Conversion of SAM files to BAM files was done using SAMtools (Li *et al.*, 2009). Deduplication was done using Picard (http://broadinstitute.github.io/picard).

Further processing of the WT versus mutant pooled experiment samples. The following steps are exclusive for the sequence processing of the WT versus mutant pooled experiment. At this point, we attempted two parallel approaches to call variants. Given that there was not any indication as to the nature of the mutation (SNP, long vs. short insertion, deletion, duplication), we decided to use both the Genome Analysis Toolkit (GATK) variant caller (DePristo *et al.*, 2011) and Pindel (Ye *et al.*, 2009).

GATK. GATK base recalibration was performed using The Supplemental VCF file including SNVs, and small Indels from Gallaher *et al.* (2015) was used for the BQSR step. GATK Haplotype Caller followed by GATK GenotypeGVCF commands were performed to get a file with SNPs and Indels. These were then separated to generate a file with SNPS and another with Indels. Using the bcftools isec (-c all) command option, the two sample pools (WT vs. MUT) were compared with one another to get variants unique to each sample. The variants unique to the mutant pool were further filtered by including only variants with GQ ≥ 20 and AF ≥ 0.9. Common SNPs and Indels found in laboratory strains were removed using the http://stormo.wustl.edu/SNPlibrary/index.html database. Next, using the variant effect predictor, snpEff (Cingolani *et al.*, 2012), only alleles with a High and Moderate effect were included.

Pindel. The deduplicated BAM files for each sample, WT and mutant, were inputted into the Pindel software, which gave separate files for different types of genetic lesions as the output. The short insertions and deletions files were filtered to include only alleles whereby the genotype was 1/1 in one pool and 0/0 in the other.

The final filtered SNP file from the GATK pipeline contained two variants. The final filtered Indel file from the GATK pipeline contained 10 variants. The Pindel file containing deletion variants had eight different variants. We used the Integrated Genomics Viewer (IGV) (Thorvaldsdottir *et al.*, 2013) to directly compare the pool alignments to each other and the reference genome, focusing on the regions of interest provided by the final filtered variant files. We found that most of the unique variants called in the mutant sample were in fact common between the two samples or common to known variants listed in Phytozome. The 5-base-pair deletion called in chromosome 6, position 4,097,271, was interesting because it was the only variant called both in the filtered Pindel deletion file and in the final, filtered GATK variant file. In addition, the aligned reads very clearly demonstrated that the deletion could be seen only in the mutant pool and not in the WT pool. Interestingly, one of the two SNPs from the final filtered SNP variant file produced by GATK, chromosome_6 position 3344626, C to A, was only found in the mutant pool when aligned reads were viewed through IGV. This genotype has been reported previously as it was present in the Phytozome variation list for the gene Cre06.g277500. Therefore, we did not believe that it was the mutation leading to the short-flagellar phenotype. We do believe that this is worth noting because it is located relatively close to the 5-base-pair deletion, indicating that these mutations are linked.

Further processing of the varying genomic ratios of shf1 allele pool sample. Given that the *shf1* allele was previously mapped to linkage group VI near the centromere, we had a strong suspicion that the gene affected in this mutant was Crescerin. Therefore, we took a biased but quick approach to looking for the causative mutation

by focusing on the Crescerin gene. The BAM file–generated SAMtools conversion was used to view the reads in IGV. Scrolling through the gene, there were two notable variants. In chromosome 6, position 4,096,059, there was a single base change from T to A, with a frequency of 74% A and 26% T. In chromosome 6, position 4,096,059, there was a base pair deletion that accounted for 28% of the aligned reads. The T to A nonsense mutation leads to an early stop codon, and the base pair deletion leads to a frame shift in the open reading frame that leads to an early stop codon. We infer that the short-flagellar phenotype in *shf1-277* is due to the T to A nonsense mutation and in *shf1-253* it is due to the single base deletion, because the approximate input of each genome in the sequenced pool (65 and 30%) roughly parallels the observed allele frequency, 74 and 28%, respectively. We were not able to obtain a predicted allele for *shf1-236*, presumably because 5% of the pool was under the limit of sensitivity.

Crescerin/SHF1 gene cloning (pKPL_1- SHF-A)

A hybrid approach of stitching together gDNA and cDNA was used to generate the template Crescerin/SHF1 transgene plasmid (pKPL_1), which was then used to generate pKPL_2 and pKPL_3. Given the high GC content and the size of the gene (~10.4 kb including a 500-base-pair promoter region, 5'UTR-exon1-exon14-3'UTR), the final transgene was a result of piecewise stitching via In-fusion by way of intermediate plasmids. This approach was used because the original approach, a one-shot In-fusion reaction with several DNA pieces, failed to give any colonies. Two intermediate plasmids were generated through In-Fusion in a sequential manner that then led to one of the final transgene plasmids (pKPL_1) used for transformation of cells. Supplemental_Table_2 has a thorough description of all the gene regions amplified. Phusion Hotstart II polymerase (Thermofisher) was used to generate all the inserts. In the following steps each amplicon generated by either PCR amplification or vector digestion was isolated and extracted from a 1% agarose gel through the NucleoSpin Gel (Macherey-Nagel) and PCR Clean-Up Kit (Takara), and then In-Fusion (Takara) was used to combine these homologous inserts and linearized vectors. In brief, the first intermediate plasmid was generated by fusing three inserts with homologous overhangs and a linearized vector that contains a hygromycin resistance gene for selection. This first intermediate plasmid was linearized via *Eco*RV (New England Biolabs-NEB) digestion, and two inserts were added to it by In-Fusion to generate the second intermediate plasmid. The final plasmid (pKPL_1) was generated by linearizing the second intermediate plasmid with *Eco*RV digestion and adding two more inserts. One of these two final inserts included a 3x-FLAG tag inserted in-frame after glycine 1289. Sanger sequencing was used to verify the sequence of pKPL_1.

Additional Crescerin/SHF1 gene tagging (pKPL_2 [SHF-B])

To generate a construct with an mCherry + 3x-HA tag at the same location as the tag in pKPL_1 (glycine 1289), the pKPL_1 plasmid was used as PCR template and linearized vector while the pBR9-mCherry plasmid was used to amplify the mCherry coding region (Rasala *et al.*, 2013). Supplemental_Table_2 has a thorough description of all the gene regions amplified. In brief, the pKPL_1 plasmid was linearized with *Eco*NI (NEB) and *Sap*I (NEB) to generate a 11,989-base-pair region with most of the Crescerin gene. Three inserts generated by PCRs were added to this linearized vector in one In-Fusion reaction. The final plasmid, pKPL_2, is essentially the same as pKPL_1 with the exception that after glycine 1289, there is an mCherry + 3x-HA tag rather than a 3x-FLAG. Sanger sequencing was used to verify the sequence of pKPL_2.

Additional Crescerin gene tagging (pKPL_1-CrGFP [SHF-C])

For the pKPL_1-CrGFP plasmid, the codon-optimized *Chlamydomonas* GFP tag was amplified by PCR from the plasmid pBR9 GFP (Rasala *et al.*, 2013) with primers (CrCHE12-CrGFP:IFS-2 and CrGFP-CrCHE12:IFR-2) and inserted into a unique *Stu*I site in the pKPL_1 plasmid. Supplemental_Table_2 has a thorough description of the primer sequences. The GFP PCR insert was added to the *Stu*I linearized vector in one In-Fusion reaction. The final plasmid, pKPL_1-CrGFP, is essentially the same as pKPL_1 with the exception that in addition to the 3x-FLAG after glycine 1289 there is a GFP tag after phenylalanine 9.

Sequence alignment and phylogenetic tree

Crescerin/SHF1 homologues from different organisms were identified using BLASTP (Altschul *et al.*, 1990). NCBI accession numbers of these homologues that were used for the phylogenetic tree analysis are listed in sheet 3 of Supplemental_Table_1. The phylogenetic analysis was done using the algorithms of MEGAX (Kumar *et al.*, 2018). The evolutionary tree was inferred by using the maximum-likelihood method and JTT matrix-based model (Jones *et al.*, 1992). The sequence alignment between the *M. musculus* and *C. reinhardtii* proteins was done using T-coffee, http://tcoffee.crg.cat/apps/tcoffee/index.html (Notredame *et al.*, 2000). Secondary structure prediction was done using the PSIPRED servers (McGuffin *et al.*, 2000; Buchan *et al.*, 2013).

Transgene nuclear transformation

The Crescerin/SHF1 transgene was integrated into the nuclear genome with the NEPA21 electroporator (Nepagene) using the settings found to be most effective in Yamano *et al.* (2013) and the protocol described in Perlaza *et al.* (2019). Briefly, 5–8 µl of nonlinearized, plasmid DNA at a concentration of 1–2 mg/ml was mixed with 5 µl of salmon sperm DNA (10 mg/ml) (Thermofisher Scientific) before electroporation. *Chlamydomonas* cells in the logarithmic stage were spun down and resuspended in TAP media and placed in a cuvette in a final volume of 50 µl. Electroporation parameters are thoroughly described in Perlaza *et al.* (2019). Transformants were isolated on TAP agar containing 20 µg/ml hygromycin.

Screening of transformants grown in hygromycin plates

Typically, any *shf* mutant transformed with a Crescerin/SHF1 plasmid was screened by selecting ~10–20 colonies from the hygromycin plates, isolating them onto fresh hygromycin TAP plates (20 µg/ml), and then looking at their flagella using the Deltavision. This first pass allowed us to narrow down the samples needed for epitope immunoblot verification. Every transformant that we selected as having WT-like flagella also expressed Crescerin/SHF1. For the WT background transformations with the Crescerin/SHF1 plasmids, we did not prescreen transformants because we did not know what to expect. Instead, we selected ~10–20 colonies and directly analyzed them through epitope immunoblots.

Immunofluorescence microscopy

Immunofluorescence experiments on *Chlamydomonas* strains were done essentially as described previously (Wood *et al.*, 2012) with several deviations as described below. Cells were allowed to adhere onto poly-lysine–coated coverslips for a maximum of 3 min because flagella begin to curl if left for longer. Both primary and secondary antibodies were diluted in 20% of the blocking buffer (in phosphate-buffered saline [PBS]). The cells were incubated in a mixture of primary antibodies, anti–α-tubulin rabbit polyclonal (Abcam 18251) (1:1000) and anti-HA tag mouse monoclonal antibody ([HA.C5]

Abcam ab18181) (1:400), for 1 h at room temperature (RT). The fluorophore-conjugated secondary antibodies, Thermofisher Alexa Fluor Plus 488 goat anti-mouse (1:1000) and Thermofisher Alexa Fluor 546 goat anti-rabbit (1:1000), were diluted in 20% blocking buffer and mounted in Vectashield medium. Laser scanning confocal microscopy was performed using a Nikon Ti inverted fluorescence microscope with CSU-22 spinning-disk confocal with the Plan Apo VC 100×/1.4 oil objective lens.

Image processing and analysis

Image processing. Multichannel z-stacks were imported in FIJI (Schindelin *et al.*, 2012) as 32-bit TIFFs, and Sum Slices z-projection was performed on composite images. Single cells were cropped for analysis if they had at least one intact flagellum, at least 1.5 µm long, which did not overlap with any other fluorescent structure. Flagellar intensity linescans were taken from base to tip of each flagellum for tubulin and Crescerin-HA channels using the Segmented Line tool and Plot Profile function in FIJI. Measurements were saved as separate .csv files for each channel. Background fluorescence for each channel was taken as the mean intensity of a circular area of 1–2 µm diameter near the cell using the Measurement tool. Background measurements were saved as one .csv file containing measurements for all flagella in the data set. Image metadata including z-sizes of stacks were extracted in Python and saved in a separate file.

Image analysis. Data formatting, processing, statistical analysis, and plotting were performed in Python and Microsoft Excel. Intensity and position values from each flagellum were preprocessed in the following steps: 1) positions normalized to total flagellar length ("normalized x"), 2) Sum Slices intensities divided by z-size for Average Slices intensity, 3) Background subtraction of Sum Slices and Average Slices intensities, 4) HA normalized to tubulin at each point for Average Slices intensities (HA:TUB), in order to control for artifacts such as flagellar curling at the tip (resulting in locally increased tubulin and HA-Crescerin intensity), and 5) moving average smoothing of HA:TUB. Based on HA:TUB intensity, mean and SD of flagellar intensities, as well as flagellar length, were pooled into a common file.

For analysis of HA:TUB puncta in flagella, puncta detection was performed as follows. Binary thresholding (average + 1.4 SD) of smoothed HA:TUB intensity for each flagellum was performed. All intensities below the threshold were averaged for the mean baseline intensity. A new threshold of 1 + 1.25 SD of the baseline intensity was applied to the smoothed HA:TUB data. Consecutive regions above the threshold were recorded as a series of puncta start and end positions. Puncta consisting of only one point were removed. Within the boundaries of each punctum, the mean, SD, max, and sum intensity were calculated based on unsmoothed HA:TUB intensity. Puncta size, midpoint position, max position, mean and max intensity enrichment (normalized to mean baseline intensity), and number of puncta per flagellum were calculated. Finally, the presence of puncta at the flagellar tip was scored if the final point was inside of a punctum (final point of thresholded binary equal to 1).

Note that five flagella from steady state were not plotted in Figure 6B because their lengths were shorter than 5 µm, which could mean that they correspond to cells actively regenerating flagella due to mechanical shearing or they may have been cut off during fixation.

Modeling

To model potential roles of for Crescerin/SHF1 in flagellar length control, we started with a computational model that we previously developed for studying the effect of katanin on flagellar length control, in which the length of flagellar microtubules is represented by a differential equation for flagellar length combined with a stochastic model for cytoplasmic microtubule dynamics (Kannegaard *et al.*, 2014). Our model is identical to the previously described model except that we modified it to explicitly model soluble tubulin within the flagellar compartment. At each time step, the current concentration of soluble tubulin in the cell body is used to calculate the fraction of IFT particles entering the flagella that have tubulin bound. This calculation assumes saturable binding with a dissociation constant that is a parameter of the model. A second parameter of the model is the number of tubulin-binding sites per IFT particle. IFT particles are then modeled as entering the flagellum at a rate proportional to 1/L, based on previous observations (Engel *et al.*, 2009; Ludington *et al.*, 2013). As IFT particles enter the flagellum, they release their tubulin cargo. The concentration of tubulin is described by a differential equation that takes into account the rate at which new tubulin is delivered by IFT and the rate at which tubulin is assembled onto the growing axoneme. The net flagellar growth rate is calculated as the difference between an assembly and disassembly term. The disassembly term is a length-independent constant, consistent with previous observations (Marshall and Rosenbaum, 2001). Based on the assumption that tubulin removed from the axoneme via disassembly is in the GDP-bound form and hence incapable of reassembly, the tubulin produced by disassembly is added back to the cytoplasmic pool. The assembly rate is a linear function of the tubulin concentration in the flagellum, with the slope and intercept being two adjustable parameters of the model. Flagellar length is updated using an Euler method with a timestep of 0.05 s. At each time point, after the tubulin concentration and flagellar lengths are updated, a stochastic simulation is carried out to determine how the lengths of a set of 10 cytoplasmic microtubules may have changed during the time step. This simulation is based on a previously described simplified model of tubulin dynamics (Gregoretti *et al.*, 2006) augmented to include the action of a microtubule-depolymerizing kinesin at the tip and a microtubule-severing protein along the length, as previously described (Kannegaard *et al.*, 2014). This last step updates the free tubulin concentration that will then be used to calculate import at the next time step.

Simulations start with an initial condition of length equal to 0.1 µm (we avoid 0 to prevent division by zero), and the simulation is allowed to run for a specified number of iterations, sufficient to reach a visible steady state. This first part of the simulation provides a prediction for the steady-state flagellar length. Next, the flagellar length is reset to 0.1 and the total quantity of available tubulin is reduced by a quantity equivalent to that stored in the two flagella. The flagella are now simulated regrowing in the presence of this reduced pool, in order to simulate the experiments in which regeneration is done in the absence of protein synthesis. This second phase is allowed to run to steady state, allowing us to calculate the predicted flagellar length after regeneration in cycloheximide.

We modeled two different possible effects of the Crescerin/SHF1 mutation. In the first scenario, we make the assumption that Crescerin/SHF1 is acting as a microtubule polymerase to catalyze microtubule assembly at the flagellar tip. To represent the effect of a Crescerin/SHF1 mutation, we reduced the slope of the elongation versus tubulin concentration function in the assembly term of the flagellar length rate equation. In the second scenario, we make the assumption that Crescerin/SHF1 is acting primarily as a tubulin-recruiting factor for IFT particles as they enter the flagellum. To represent the effect of a Crescerin/SHF1 mutation in this scenario, we reduced the number of tubulin-binding sites in the model and also increased the dissociation

constant for tubulin binding, to represent the idea that Crescerin/SHF1 can bind tubulin more tightly than the built-in tubulin-binding sites on the IFT particles (Bhogaraju *et al*., 2013a).

In an attempt to determine parameters under which the polymerase model could account for our observations, we systematically changed each parameter in the model other than the elongation rate parameter that reflects the proposed polymerase activity. Specifically, we changed the flagellar disassembly rate, the critical concentration of tubulin for flagellar assembly, the cytoplasmic microtubule-severing rate mediated by katanin, and the cytoplasmic microtubule turnover rate. These parameter changes each resulted in a changed steady-state length, but when the elongation rate constant was then swept to simulate a mutation in a presumed polymerase function, it was found that any reduction in elongation rate sufficient to produce a half-length flagellum at steady state did not permit subsequent reassembly of flagella in the absence of new protein synthesis within the model. We speculate that this effect is due to the fact that when the elongation rate is reduced, the flagellum spends more time growing at a shorter length. Because the rate of IFT particle transport is proportional to 1/L in our model, the import of tubulin is much higher in very short flagella. Because elongation rate mutants spend more time at these short lengths, they are able to sequester a larger quantity of tubulin, which is then lost when flagellar severing is simulated.

We note that this model is a coarse-grained, highly simplified model of tubulin behavior in flagellar length dynamics. Many key biochemical parameters, such as binding affinities and absolute protein numbers, remain unknown for many parts of the flagellar assembly system. However, as such values become available from experiments in the future, they can be readily incorporated into the existing modeling framework to constrain possible models.

Denaturing protein extract and immunoblot assay

Cell cultures were grown to mid–log phase and subsequently spun down at 3000 × *g* for 8 min. The pellets were resuspended in 150 µl of TAP. An equal volume of 0.2 M NaOH was added to the pellets, vortexed at RT for 5 min, and pelleted at 15,000 × *g* for 5 min. The supernatant was removed, the pellet was resuspended in ~200 µl of SDS sample buffer (0.06 M Tris-HCl, pH 6.8, 5% glycerol, 2% SDS, 4% 2-mercaptoethanol, 0.0025% bromophenol blue), boiled for 5 min, and then pelleted again. Proteins were separated by SDS–PAGE using Criterion Precast Gels (Bio-Rad) and transferred onto nitrocellulose membrane, 0.2 µm pore. Nonspecific signal was blocked with phosphate buffered saline with 0.1% Tween 20 detergent (PBS-T) supplemented with 5% instant nonfat dry milk for 1 h at RT or overnight at 4°C. All primary and secondary antibodies were diluted in this blocking buffer. The following antibodies (at the indicated dilution) were used for this publication: monoclonal mouse anti-Flag (1:2000) (M2; Sigma F1804) and monoclonal mouse anti–α-tubulin (1:5000) (Sigma; #T6074). To detect the primary antibodies, horseradish peroxidase–conjugated anti-rabbit and anti-mouse secondary antibodies (Promega) were used at dilution 1:10,000 in PBS-T supplemented with 5% instant nonfat dry milk for 1 h at RT. In between the incubation with primary and secondary antibodies and after the incubation with the secondary antibody, three washes of ~10 min each time, at RT, were performed using PBS-T in 5% instant nonfat dry milk. The enhanced chemiluminescence (ECL) method was applied to develop the signal. For most immunoblot analysis, the SuperSignal West Dura Extended Duration Substrate kit (Thermofisher Scientific) was used according to the manufacturer's directions. The ECL signal was detected with the LI-COR Odyssey imaging system.

Flagellar regeneration

pH shock was used to induce flagellar regeneration. The pH of cell cultures was adjusted to pH 4.5 with 0.5 N acetic acid and incubated for 1 min to deflagellate, and then the pH was returned to pH 7.0 with 0.5 N KOH. Immediately after this, the cells were spun down for ~3 min at 500 × *g* and resuspended in the same starting volume of TAP or M1 media. For time point experiments, cells were fixed in a final concentration of 1.5% glutaraldehyde. Flagella were imaged using differential interference contrast (DIC) microscopy (Deltavision) at 100× magnification. Then, flagellar lengths were measured using the line segment tracing tool on the ImageJ software.

LiCl elongation and cycloheximide regeneration experiments

For the LiCl experiments, strains were grown in TAP media to ~2–4 × 10^6 cells/ml. A stock solution of 7.5 M LiCl in water was diluted in TAP medium to a final concentration of 50 mM of LiCl. The cell culture was then diluted twofold by mixing in an equal volume of 50 mM LiCl medium. In experiments using cycloheximide, cells were grown in TAP media to ~6 × 10^6 cells/ml and then cycloheximide was added to a final concentration of 12.5 µg/ml from a stock solution of 10 mg/ml in water. The drug was added to the cells 15 min before pH shock. Immediately after pH shock, cells were spun down for 3 min at 500 × *g* and resuspended in TAP media containing 12.5 µg/ml cycloheximide. For both the LiCl and cycloheximide experiments an equal volume of water was added as a control for drug addition.

ACKNOWLEDGMENTS

We thank members of the Marshall lab for helpful discussions and Hiro Ishikawa for careful reading of the manuscript. This work was supported by National Institutes of Health grant R35 GM130327 (W.F.M.).

REFERENCES

Al-Bassam J, Chang F (2011). Regulation of microtubule dynamics by TOG-domain proteins XMAP215/Dis1 and CLASP. Trends Cell Biol 21, 604–614.

Al-Bassam J, Kim H, Brouhard G, van Oijen A, Harrison SC, Chang F (2010). CLASP promotes microtubule rescue by recruiting tubulin dimers to the microtubule. Dev Cell 19, 245–258.

Al-Bassam J, Larsen NA, Hyman AA, Harrison SC (2007). Crystal structure of a TOG domain: conserved features of XMAP215/Dis1-family TOG domains and implications for tubulin binding. Structure 15, 355–362.

Al-Bassam J, van Breugel M, Harrison SC, Hyman A (2006). Stu2p binds tubulin and undergoes an open-to-closed conformational change. J Cell Biol 172, 1009–1022.

Albee AJ, Kwan AL, Lin H, Granas D, Stormo GD, Dutcher SK (2013). Identification of cilia genes that affect cell-cycle progression using whole-genome transcriptome analysis in Chlamydomonas reinhardtti. G3 3, 979–991.

Al-Jassar C, Andreeva A, Barnabas DD, McLaughlin SH, Johnson CM, Yu M, van Breugel M (2017). The ciliopathy-associated Cep104 protein interacts with tubulin and Nek1 kinase. Structure 25, 146–156.

Altschul SF, Gish W, Miller W, Myers EW, Lipman DJ (1990). Basic local alignment search tool. J Mol Biol 215, 403–410.

Asleson CM, Lefebvre PA (1998). Genetic analysis of flagellar length control in Chlamydomonas reinhardtii: a new long-flagella locus and extragenic suppressor mutations. Genetics 148, 693–702.

Avasthi P, Onishi M, Karpiak J, Yamamoto R, Mackinder L, Jonikas MC, Sale WS, Shoichet B, Pringle JR, Marshall WF (2014). Actin is required for IFT regulation in Chlamydomonas reinhardtii. Curr Biol 24, 2025–2032.

Bacaj T, Lu Y, Shaham S (2008). The conserved proteins CHE-12 and DYF-11 are required for sensory cilium function in Caenorhabditis elegans. Genetics 178, 989–1002.

Barsel SE, Wexler DE, Lefebvre PA (1988). Genetic analysis of long-flagella mutants of Chlamydomonas reinhardtii. Genetics 118, 637–648.

Berman SA, Wilson NF, Haas NA, Lefebvre PA (2003). A novel MAP kinase regulates flagellar length in Chlamydomonas. Curr Biol 13, 1145–1149.
Bhogaraju S, Cajanek L, Fort C, Blisnick T, Weber K, Taschner M, Mizuno N, Lamla S, Bastin P, Nigg EA, Lorentzen E (2013a). Molecular basis of tubulin transport within the cilium by IFT74 and IFT81. Science 341, 1009–1012.
Bhogaraju S, Engel BD, Lorentzen E (2013b). Intraflagellar transport complex structure and cargo interactions. Cilia 2, 10.
Bhogaraju S, Weber K, Engel BD, Lechtreck K-F, Lorentzen E (2014). Getting tubulin to the tip of the cilium: one IFT train, many different tubulin cargo-binding sites? Bioessays 36, 463–467.
Bolger AM, Lohse M, Usadel B (2014). Trimmomatic: a flexible trimmer for Illumina sequence data. Bioinformatics 30, 2114–2120.
Bradley BA, Quarmby LM (2005). A NIMA-related kinase, Cnk2p, regulates both flagellar length and cell size in Chlamydomonas. J Cell Sci 118, 3317–3326.
Brouhard GJ, Stear JH, Noetzel TL, Al-Bassam J, Kinoshita K, Harrison SC, Howard J, Hyman AA (2008). XMAP215 is a processive microtubule polymerase. Cell 132, 79–88.
Buchan DWA, Minneci F, Nugent TCO, Bryson K, Jones DT (2013). Scalable web services for the PSIPRED Protein Analysis Workbench. Nucleic Acids Res 41, W349–W357.
Byrnes AE, Slep KC (2017). TOG-tubulin binding specificity promotes microtubule dynamics and mitotic spindle formation. J Cell Biol 216, 1641–1657.
Chan Y-HM, Marshall WF (2012). How cells know the size of their organelles. Science 337, 1186–1189.
Chen X, Zaro JL, Shen W-C (2013). Fusion protein linkers: property, design and functionality. Adv Drug Deliv Rev 65, 1357–1369.
Cingolani P, Platts A, Wang LL, Coon M, Nguyen T, Wang L, Land SJ, Lu X, Ruden DM (2012). A program for annotating and predicting the effects of single nucleotide polymorphisms, SnpEff: SNPs in the genome of Drosophila melanogaster strain w1118; iso-2; iso-3. Fly 6, 80–92.
Craft JM, Harris JA, Hyman S, Kner P, Lechtreck KF (2015). Tubulin transport by IFT is upregulated during ciliary growth by a cilium-autonomous mechanism. J Cell Biol 208, 223–237.
Craft Van De Weghe J, Harris JA, Kubo T, Witman GB, Lechtreck KF (2020). Diffusion rather than IFT likely provides most of the tubulin required for axonemal assembly. J Cell Sci 133, jcs249805.
Czarnecki PG, Shah JV (2012). The ciliary transition zone: from morphology and molecules to medicine. Trends Cell Biol 22, 201–210.
Das A (2016). The Crescerin Protein Family Uses Arrayed Tog Domains to Regulate Microtubules in Cilia. PhD Thesis. University of North Carolina at Chapel Hill Graduate School.
Das A, Dickinson DJ, Wood CC, Goldstein B, Slep KC (2015). Crescerin uses a TOG domain array to regulate microtubules in the primary cilium. Mol Biol Cell 26, 4248–4264.
DePristo MA, Banks E, Poplin R, Garimella KV, Maguire JR, Hartl C, Philippakis AA, del Angel G, Rivas MA, Hanna M, *et al.* (2011). A framework for variation discovery and genotyping using next-generation DNA sequencing data. Nat Genet 43, 491–498.
Dutcher SK, Li L, Lin H, Meyer L, Giddings TH Jr, Kwan AL, Lewis BL (2012). Whole-genome sequencing to identify mutants and polymorphisms in Chlamydomonas reinhardtii. G3 2, 15–22.
Engel BD, Ishikawa H, Wemmer KA, Geimer S, Wakabayashi K, Hirono M, Craige B, Pazour GJ, Witman GB, Kamiya R, Marshall WF (2012). The role of retrograde intraflagellar transport in flagellar assembly, maintenance, and function. J Cell Biol 199, 151–167.
Engel BD, Ludington WB, Marshall WF (2009). Intraflagellar transport particle size scales inversely with flagellar length: revisiting the balance-point length control model. J Cell Biol 187, 81–89.
Ford MM, Lawrence SR 2nd, Werth EG, McConnell EW, Hicks LM (2020). Label-free quantitative phosphoproteomics for algae. Methods Mol Biol 2139, 197–211.
Fox JC, Howard AE, Currie JD, Rogers SL, Slep KC (2014). The XMAP215 family drives microtubule polymerization using a structurally diverse TOG array. Mol Biol Cell 25, 2375–2392.
Gallaher SD, Fitz-Gibbon ST, Glaesener AG, Pellegrini M, Merchant SS (2015). Chlamydomonas genome resource for laboratory strains reveals a mosaic of sequence variation, identifies true strain histories, and enables strain-specific studies. Plant Cell 27, 2335–2352.
Gregoretti IV, Margolin G, Alber MS, Goodson HV (2006). Insights into cytoskeletal behavior from computational modeling of dynamic microtubules in a cell-like environment. J Cell Sci 119, 4781–4788.
Hao L, Thein M, Brust-Mascher I, Civelekoglu-Scholey G, Lu Y, Acar S, Prevo B, Shaham S, Scholey JM (2011). Intraflagellar transport delivers tubulin isotypes to sensory cilium middle and distal segments. Nat Cell Biol 13, 790–798.
Höög JL, Lacomble S, O'Toole ET, Hoenger A, McIntosh JR, Gull K (2014). Modes of flagellar assembly in Chlamydomonas reinhardtii and Trypanosoma brucei. eLife 3, e01479.
Iomini C, Babaev-Khaimov V, Sassaroli M, Piperno G (2001). Protein particles in Chlamydomonas flagella undergo a transport cycle consisting of four phases. J Cell Biol 153, 13–24.
Ishikawa H, Ide T, Yagi T, Jiang X, Hirono M, Sasaki H, Yanagisawa H, Wemmer KA, Stainier DY, Qin H, *et al.* (2014). TTC26/DYF13 is an intraflagellar transport protein required for transport of motility-related proteins into flagella. eLife 3, e01566.
Jarvik JW, Reinhart FD, Kuchka MR, Adler SA (1984). Altered flagellar size-control in shf-1 short-flagella mutants of Chlamydomonas reinhardtii. J Protozool 31, 199–204.
Jiang X (2017). Eukaryotic Flagellar Assembly: Insights Learned from Intraflagellar Transport (IFT) and Small GTPase ARL3. PhD Thesis. Texas A&M University.
Johnson KA, Rosenbaum JL (1992). Polarity of flagellar assembly in Chlamydomonas. J Cell Biol 119, 1605–1611.
Jones DT, Taylor WR, Thornton JM (1992). The rapid generation of mutation data matrices from protein sequences. Comput Appl Biosci 8, 275–282.
Kannegaard E, Rego EH, Schuck S, Feldman JL, Marshall WF (2014). Quantitative analysis and modeling of katanin function in flagellar length control. Mol Biol Cell 25, 3686–3698.
Kathir P, LaVoie M, Brazelton WJ, Haas NA, Lefebvre PA, Silflow CD (2003). Molecular map of the Chlamydomonas reinhardtii nuclear genome. Eukaryot Cell 2, 362–379.
Keller LR, Schloss JA, Silflow CD, Rosenbaum JL (1984). Transcription of alpha- and beta-tubulin genes in vitro in isolated Chlamydomonas reinhardi nuclei. J Cell Biol 98, 1138–1143.
Kozminski KG, Johnson KA, Forscher P, Rosenbaum JL (1993). A motility in the eukaryotic flagellum unrelated to flagellar beating. Proc Natl Acad Sci USA 90, 5519–5523.
Kubo T, Brown JM, Bellve K, Craige B, Craft JM, Fogarty K, Lechtreck KF, Witman GB (2016). Together, the IFT81 and IFT74 N-termini form the main module for intraflagellar transport of tubulin. J Cell Sci 129, 2106–2119.
Kuchka MR, Jarvik JW (1987). Short-flagella mutants of Chlamydomonas reinhardtii. Genetics 115, 685–691.
Kumar S, Stecher G, Li M, Knyaz C, Tamura K (2018). MEGA X: Molecular Evolutionary Genetics Analysis across computing platforms. Mol Biol Evol 35, 1547–1549.
Latour BL, Van De Weghe JC, Rusterholz TD, Letteboer SJ, Gomez A, Shaheen R, Gesemann M, Karamzade A, Asadollahi M, Barroso-Gil M, *et al.* (2020). Dysfunction of the ciliary ARMC9/TOGARAM1 protein module causes Joubert syndrome. J Clin Invest 130, 4423–4439.
Lefebvre PA, Nordstrom SA, Moulder JE, Rosenbaum JL (1978). Flagellar elongation and shortening in Chlamydomonas. IV. Effects of flagellar detachment, regeneration, and resorption on the induction of flagellar protein synthesis. J Cell Biol 78, 8–27.
Lefebvre PA, Rosenbaum JL (1986). Regulation of the synthesis and assembly of ciliary and flagellar proteins during regeneration. Annu Rev Cell Biol 2, 517–546.
Li H, Durbin R (2009). Fast and accurate short read alignment with Burrows–Wheeler transform. Bioinformatics 25, 1754–1760.
Li H, Handsaker B, Wysoker A, Fennell T, Ruan J, Homer N, Marth G, Abecasis G, Durbin R, 1000 Genome Project Data Processing Subgroup (2009). The Sequence Alignment/Map format and SAMtools. Bioinformatics 25, 2078–2079.
Li X, Patena W, Fauser F, Jinkerson RE, Saroussi S, Meyer MT, Ivanova N, Robertson JM, Yue R, Zhang R, *et al.* (2019). A genome-wide algal mutant library and functional screen identifies genes required for eukaryotic photosynthesis. Nat Genet 51, 627–635.
Li X, Zhang R, Patena W, Gang SS, Blum SR, Ivanova N, Yue R, Robertson JM, Lefebvre PA, Fitz-Gibbon ST, *et al.* (2016). An indexed, mapped mutant library enables reverse genetics studies of biological processes in Chlamydomonas reinhardtii. Plant Cell 28, 367–387.
Lin H, Nauman NP, Albee AJ, Hsu S, Dutcher SK (2013). New mutations in flagellar motors identified by whole genome sequencing in Chlamydomonas. Cilia 2, 14.
Louka P, Vasudevan KK, Guha M, Joachimiak E, Wloga D, Tomasi RF-X, Baroud CN, Dupuis-Williams P, Galati DF, Pearson CG, *et al.* (2018). Proteins that control the geometry of microtubules at the ends of cilia. J Cell Biol 217, 4298–4313.

Lucker BF, Miller MS, Dziedzic SA, Blackmarr PT, Cole DG (2010). Direct interactions of intraflagellar transport complex B proteins IFT88, IFT52, and IFT46. J Biol Chem 285, 21508–21518.
Ludington WB, Ishikawa H, Serebrenik YV, Ritter A, Hernandez-Lopez RA, Gunzenhauser J, Kannegaard E, Marshall WF (2015). A systematic comparison of mathematical models for inherent measurement of ciliary length: how a cell can measure length and volume. Biophys J 108, 1361–1379.
Ludington WB, Wemmer KA, Lechtreck KF, Witman GB, Marshall WF (2013). Avalanche-like behavior in ciliary import. Proc Natl Acad Sci USA 110, 3925–3930.
Luo M, Cao M, Kan Y, Li G, Snell W, Pan J (2011). The phosphorylation state of an aurora-like kinase marks the length of growing flagella in Chlamydomonas. Curr Biol 21, 586–591.
Marshall WF, Qin H, Brenni MR, Rosenbaum JL (2005). Flagellar length control system: testing a simple model based on intraflagellar transport and turnover. Mol Biol Cell 16, 270–278.
Marshall WF, Rosenbaum JL (2001). Intraflagellar transport balances continuous turnover of outer doublet microtubules: implications for flagellar length control. J Cell Biol 155, 405–414.
Matsuura K, Lefebvre PA, Kamiya R, Hirono M (2002). Kinesin-II is not essential for mitosis and cell growth in Chlamydomonas. Cell Motil Cytoskeleton 52, 195–201.
McGuffin LJ, Bryson K, Jones DT (2000). The PSIPRED protein structure prediction server. Bioinformatics 16, 404–405.
McVittie A (1972). Flagellum mutants of Chlamydomonas reinhardii. J Gen Microbiol 71, 525–540.
Merchant SS, Prochnik SE, Vallon O, Harris EH, Karpowicz SJ, Witman GB, Terry A, Salamov A, Fritz-Laylin LK, Maréchal-Drouard L, *et al*. (2007). The Chlamydomonas genome reveals the evolution of key animal and plant functions. Science 318, 245–250.
Morbidoni V, Agolini E, Slep KC, Pannone L, Zuccarello D, Cassina M, Grosso E, Gai G, Salviati L, Dallapiccola B, *et al*. (2021). Biallelic mutations in the TOGARAM1 gene cause a novel primary ciliopathy. J Med Genet 58, 526–533.
Nakamura S, Takino H, Kojima MK (1987). Effect of lithium on flagellar length in Chlamydomonas reinhardtii. Cell Struct Funct 12, 369–374.
Notredame C, Higgins DG, Heringa J (2000). T-Coffee: a novel method for fast and accurate multiple sequence alignment. J Mol Biol 302, 205–217.
Pan J, Wang Q, Snell WJ (2004). An aurora kinase is essential for flagellar disassembly in Chlamydomonas. Dev Cell 6, 445–451.
Pazour GJ, Agrin N, Leszyk J, Witman GB (2005). Proteomic analysis of a eukaryotic cilium. J Cell Biol 170, 103–113.
Pazour GJ, Wilkerson CG, Witman GB (1998). A dynein light chain is essential for the retrograde particle movement of intraflagellar transport (IFT). J Cell Biol 141, 979–992.
Perlaza K, Toutkoushian H, Boone M, Lam M, Iwai M, Jonikas MC, Walter P, Ramundo S (2019). The Mars1 kinase confers photoprotection through signaling in the chloroplast unfolded protein response. eLife 8, e49577.
Piao T, Luo M, Wang L, Guo Y, Li D, Li P, Snell WJ, Pan J (2009). A microtubule depolymerizing kinesin functions during both flagellar disassembly and flagellar assembly in Chlamydomonas. Proc Natl Acad Sci USA 106, 4713–4718.
Qasim Rasi M, Parker JDK, Feldman JL, Marshall WF, Quarmby LM (2009). Katanin knockdown supports a role for microtubule severing in release of basal bodies before mitosis in Chlamydomonas. Mol Biol Cell 20, 379–388.
Rasala BA, Barrera DJ, Ng J, Plucinak TM, Rosenberg JN, Weeks DP, Oyler GA, Peterson TC, Haerizadeh F, Mayfield SP (2013). Expanding the spectral palette of fluorescent proteins for the green microalga Chlamydomonas reinhardtii. Plant J 74, 545–556.
Rezabkova L, Kraatz SHW, Akhmanova A, Steinmetz MO, Kammerer RA (2016). Biophysical and structural characterization of the centriolar protein Cep104 interaction network. J Biol Chem 291, 18496–18504.
Rosenbaum JL, Child FM (1967). Flagellar regeneration in protozoan flagellates. J Cell Biol 34, 345–364.
Rosenbaum JL, Moulder JE, Ringo DL (1969). Flagellar elongation and shortening in Chlamydomonas. The use of cycloheximide and colchicine to study the synthesis and assembly of flagellar proteins. J Cell Biol 41, 600–619.
Satish Tammana TV, Tammana D, Diener DR, Rosenbaum J (2013). Centrosomal protein CEP104 (Chlamydomonas FAP256) moves to the ciliary tip during ciliary assembly. J Cell Sci 126, 5018–5029.
Schierenbeck L, Ries D, Rogge K, Grewe S, Weisshaar B, Kruse O (2015). Fast forward genetics to identify mutations causing a high light tolerant phenotype in Chlamydomonas reinhardtii by whole-genome-sequencing. BMC Genom 16, 57.
Schindelin J, Arganda-Carreras I, Frise E, Kaynig V, Longair M, Pietzsch T, Preibisch S, Rueden C, Saalfeld S, Schmid B, *et al*. (2012). Fiji: an open-source platform for biological-image analysis. Nat Methods 9, 676–682.
Slep KC (2018). A cytoskeletal symphony: owed to TOG. Dev Cell 46, 5–7.
Slep KC, Vale RD (2007). Structural basis of microtubule plus end tracking by XMAP215, CLIP-170, and EB1. Mol Cell 27, 976–991.
Song L, Dentler WL (2001). Flagellar protein dynamics in Chlamydomonas. J Biol Chem 276, 29754–29763.
Stolc V, Samanta MP, Tongprasit W, Marshall WF (2005). Genome-wide transcriptional analysis of flagellar regeneration in Chlamydomonas reinhardtii identifies orthologs of ciliary disease genes. Proc Natl Acad Sci USA 102, 3703–3707.
Tam L-W, Dentler WL, Lefebvre PA (2003). Defective flagellar assembly and length regulation in LF3 null mutants in Chlamydomonas. J Cell Biol 163, 597–607.
Tam L-W, Ranum PT, Lefebvre PA (2013). CDKL5 regulates flagellar length and localizes to the base of the flagella in Chlamydomonas. Mol Biol Cell 24, 588–600.
Tam L-W, Wilson NF, Lefebvre PA (2007). A CDK-related kinase regulates the length and assembly of flagella in Chlamydomonas. J Cell Biol 176, 819–829.
Taschner M, Weber K, Mourão A, Vetter M, Awasthi M, Stiegler M, Bhogaraju S, Lorentzen E (2016). Intraflagellar transport proteins 172, 80, 57, 54, 38, and 20 form a stable tubulin-binding IFT-B2 complex. EMBO J 35, 773–790.
Thorvaldsdottir H, Robinson JT, Mesirov JP (2013). Integrative Genomics Viewer (IGV): high-performance genomics data visualization and exploration. Brief Bioinform 14, 178–192.
Wang H, Gau B, Slade WO, Juergens M, Li P, Hicks LM (2014). The global phosphoproteome of Chlamydomonas reinhardtii reveals complex organellar phosphorylation in the flagella and thylakoid membrane. Mol Cell Proteomics 13, 2337–2353.
Wang L, Piao T, Cao M, Qin T, Huang L, Deng H, Mao T, Pan J (2013). Flagellar regeneration requires cytoplasmic microtubule depolymerization and kinesin-13. J Cell Sci 126, 1531–1540.
Wemmer K, Ludington W, Marshall WF (2020). Testing the role of intraflagellar transport in flagellar length control using length-altering mutants of Chlamydomonas. Philos Trans R Soc Lond B Biol Sci 375, 20190159.
Wemmer KA, Marshall WF (2007). Flagellar length control in Chlamydomonas—paradigm for organelle size regulation. Int Rev Cytol 260, 175–212.
Wilson NF, Lefebvre PA (2004). Regulation of flagellar assembly by glycogen synthase kinase 3 in Chlamydomonas reinhardtii. Eukaryot Cell 3, 1307–1319.
Witman GB (1975). The site of in vivo assembly of flagellar microtubules. Ann NY Acad Sci 253, 178–191.
Wood CR, Wang Z, Diener D, Zones JM, Rosenbaum J, Umen JG (2012). IFT proteins accumulate during cell division and localize to the cleavage furrow in Chlamydomonas. PLoS One 7, e30729.
Wren KN, Craft JM, Tritschler D, Schauer A, Patel DK, Smith EF, Porter ME, Kner P, Lechtreck KF (2013). A differential cargo-loading model of ciliary length regulation by IFT. Curr Biol 23, 2463–2471.
Yamano T, Iguchi H, Fukuzawa H (2013). Rapid transformation of Chlamydomonas reinhardtii without cell-wall removal. J Biosci Bioeng 115, 691–694.
Ye K, Schulz MH, Long Q, Apweiler R, Ning Z (2009). Pindel: a pattern growth approach to detect break points of large deletions and medium sized insertions from paired-end short reads. Bioinformatics 25, 2865–2871.
Yuan S, Li J, Diener DR, Choma MA, Rosenbaum JL, Sun Z (2012). Target-of-rapamycin complex 1 (Torc1) signaling modulates cilia size and function through protein synthesis regulation. Proc Natl Acad Sci USA 109, 2021–2026.
Zones JM, Blaby IK, Merchant SS, Umen JG (2015). High-resolution profiling of a synchronized diurnal transcriptome from Chlamydomonas reinhardtii reveals continuous cell and metabolic differentiation. Plant Cell 27, 2743–2769.